Summary Report on the Volatile Radionuclide and Immobilization Research for FY2011 at PNNL

Fuel Cycle Research & Development

Prepared for

U.S. Department of Energy

Separations and Waste Forms Campaign

D. M. Strachan, J. Chun, J. Matyàš, W.C. Lepry, B.J. Riley, J. V. Ryan, and P. K. Thallapally

Pacific Northwest National Laboratory

September 2011

FCRD-SWF-2011-000378

PNNL-20807

SUMMARY

Materials were developed and tested in support of the U.S. Department of Energy, Office of Nuclear Energy, Fuel Cycle Technology Separations and Waste Forms Campaign. Specifically, materials are being developed for the removal and immobilization of iodine and krypton from gaseous products of nuclear fuel reprocessing unit operations.

During FY 2011, aerogel materials were investigated for removal and immobilization of ^{129}I. Two aerogel formulations were investigated, one based on functionalized silica and the second on chalcogen-based glasses (i.e., chalcogels). A silica aerogel was tested at ORNL for total I_2 sorption capacity. It was determined to have 48 mass% capacity while having little physisorbed I_2 (I_2 not chemically bound within the aerogel). Metal organic framework (MOF) structures were investigated for the removal and storage of Kr and a new MOF with about 8 mass% capacity for Xe and Kr was formulated and tested. The selectivity can be changed from Xe > Kr to Xe < Kr simply by changing the temperature. A patent disclosure has been filed. Lastly, silicon carbide (SiC) was loaded with Kr. The diffusion of Kr in SiC was found to be less than detectable values at temperatures as high as 500°C.

CONTENTS

FIGURES

TABLES

ABBREVIATIONS

AgZ	silver-loaded zeolite
BET	Brunauer, Emmett, Teller (a method of determining surface areas accessible to a gas)
C	Cylindrical casting method
CFR	Code of Federal Register
Cg	chalcogel (sample identification prefix for chalcogels)
DF	decontamination factor
DOBDC	2,5-dihydroxybenzenedicarboxylic acid
DSC	differential scanning calorimetry
EDS	energy dispersive spectroscopy
EPA	Environmental Protection Agency
FY	fiscal year
HSAB	Hard/Soft Acid-Base
ICP-MS	inductively coupled plasma – mass spectrometer
ICSD	International Crystal Structure Database
MOF	metal organic framework
MOF	metal-organic framework
PCT	Product Consistency Test
PDF	powder diffraction file
PNNL	Pacific Northwest National Laboratory
SEM	scanning electron microscopy
TEM	transmission electron microscopy
TGA-DSC	thermogravimetric analysis
TMA	tetramethyl ammonium
ZIF	zeolitic imidazolate frameworks

1. INTRODUCTION

In his summary waste forms document, Gombert (2007) discussed many waste forms for the immobilization of volatile radionuclides. This list was narrowed in FY 2009 by Strachan et al. (2009). This report documents results from the continuation of the work discussed by Strachan (2009). Two types of aerogels, i.e., silica-based and chalcogen-based, were investigated as candidate capture media and waste form precursors for iodine immobilization. Metal organic frameworks (MOFs) were developed for the capture and storage of Kr and silicon carbide (SiC) was investigated as a candidate waste form for ^{85}Kr immobilization. The methods, results, and conclusions of these studies in FY2011 are presented here.

2. Chalcogenide-based aerogel (chalcogel) work

Lead: Brian J. Riley

Contributors: William C. Lepry and Jaehun Chun

2.1 Progress on chalcogenide-based aerogels for the removal of I_2

Progress in FY 2011 included an in-depth literature review of the previous work on I_2 removal from process off-gases, in particular for metals other than Ag that could be used. A paper entitled "Chalcogen-Based Aerogels as a Multifunctional Platform for Remediation of Radioactive Iodine" was accepted for publication in the journal *RSC Advances* (Riley et al. 2011). Additionally, two chalcogels containing no Pt were prepared and tested.

2.2 Literature studies

2.2.1 Candidate chalcogel materials and potential complimentary glass systems

In FY2011, several chalcogel families were identified as potential replacements for $Pt_2Ge_4S_{10}$. These new materials do not contain precious metals. These include:

- Sn-S-X gels, e.g., X = Sn, Sb, Zn (Oh et al. 2011; Bag et al. 2007; Kanatzidis and Bag 2008; Bag and Kanatzidis 2010)
- Ge,Sn-S gels (Bag and Kanatzidis 2010; Ruffolo and Boolchand 1985)
- Mo,W-S-X gels, e.g., X = Co, Ni, Pb, Cr, Bi (Bag et al. 2009)

2.2.1.1 Sn-S-X chalcogels

The Sn-S-X gels show great promise because they are thermally stable with low mass loss at $T \leq 600°C$ (< 8 mass%) and have high specific surfaces at ~370 m^2/g for Sn_2S_6 or ~1370 m^2/g as SiO_2 equivalent when the composition and molecular weight is renormalized ($Sn_{1.33}S_2$) to that of SiO_2 (Bag and Kanatzidis 2010). However, although these materials are thermally stable at elevated temperatures, they tend to crystalize. This could prove problematic for the long-term performance, though more work is needed to determine the glass-formation potential with various chemistries. This can be accomplished through a survey of the literature and some experimental work.

Several Sn-S have been reported (Oh et al. 2011), including SnS_4^{4-}, $Sn_2S_6^{4-}$, and $Sn_4S_{10}^{4-}$ that are present when the parent compounds, both inorganic and organic, are placed in a solvent such as formamide (CH_3NO). These moieties allow for structural and conformational flexibility for incorporating a variety of interlinking metals (such as Sn, Sb, and Zn) that yield a variety of physical and chemical properties (Bag and Kanatzidis 2010; Oh et al. 2011). It might be possible to make a glass out of Sn-S and select

Group IV or V elements, e.g., Sb. Possible reactions for chalcogel synthesis include (Bag and Kanatzidis 2010):

$$Na_4Sn_2S_6 + 2Sn\left(CH_2CO_2^-\right)_2 \rightarrow Sn_4S_6 + 4Na^+ + 4CH_2CO_2^- \quad (1.1)$$

2.2.1.2 Ge,Sn-S chalcogels

It is possible to quench Sn-S chalcogenides into the glassy state with Ge-S additions (Ruffolo and Boolchand 1985). Ruffolo and Boolchand (1985) demonstrated good glass formation in the Ge-Sn-S system with moderate additions of Sn (≤ 20 mol%). The glass formation tendency (K_{gl}) between the reported compositions in the $Ge_{40-x}Sn_xS_{60}$ system was evaluated with the Hruby criterion (Hruby 1972), seen in Equation (1.2)

$$K_{gl} = \frac{\left(T_c - T_g\right)}{\left(T_m - T_c\right)} \quad (1.2)$$

where T_g is the glass transition temperature, T_c is the crystallization temperature, and T_m is the melting temperature of the glass. The Hruby criterion is commonly used as a predictive method for non-oxide glasses like chalcogenides to estimate the required quench rate to achieve the amorphous state. A small value for ($T_c - T_g$) is not preferred because glasses with $T_c - T_g < 60$°C tend to crystallize upon cooling unless high cooling rates of are achieved (50–100 °C/s). The addition of Ge-S to the Sn-S system increases K_{gl} (Figure 1, right). However, the Sn-S is a beneficial component because it lowers the melting temperature of the glass and lowers manufacturing costs considering that Sn is ~1.5–2× less expensive than Ge of equal purities. The detriment to adding Ge-S to Sn-S is that it will increase T_m, making consolidation without iodine volatilization more difficult.

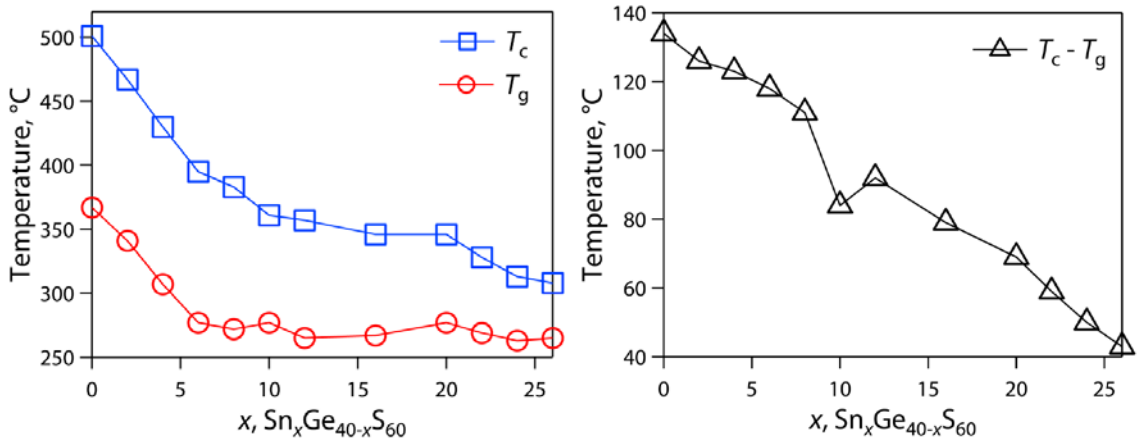

Figure 1. The T_c and T_g of various Sn-Ge-S glasses (left) along with $T_c - T_g$ plotted (right) to compare glass-formation ability.

Adding Ge to Sn gels decreases the density, thereby decreasing the volumetric waste loading. These glasses and chalcogel formulations are to be investigated in FY2012 with a combination of experiments involving Ge-S precursor $[(CH_3)_4N]_4Ge_4S_{10}$ and various Sn-S precursors such as $Na_4SnS_4 \cdot 14H_2O$, $Na_4Sn_2S_6 \cdot 14H_2O$, and $[(CH_2CH_3)_4N]_4Sn_4S_{10}$, basically reactions involving $[Sn_xS_{2x+2}]^{4-}$ clusters (Oh et al. 2011) and by analogy, $[Ge_xS_{2x+2}]^{4-}$ clusters. Suggested reactions for chalcogel synthesis close to $Ge_{40-x}Sn_xS_{60}$ chemistries where $x \sim 20$ include with Sn^{2+} as the interlinking metal to yield $Ge_{19.8}Sn_{20.2}S_{60}$ or with Ge^{2+} as the interlinking metal $Ge_{23.5}Sn_{17.5}S_{60}$ (Bag and Kanatzidis 2010; Oh et al. 2011)

2.2.1.3 Mo,W-S-X gels

The Mo,W-S gels can be made with a variety of transition metals (X). These materials can be readily and reproducibly made at a moderately low cost. The typical reactions include an inorganic synthesis route with transition metal salts, e.g., $CoCl_2 \cdot 6H_2O$, $Ni(NO_3)_2$, and $(NH_4)_2(Mo,W)S_4$. These materials are dissolved separately in a solvent, e.g., formamide, and then the solutions are combined. A variety of transition metals have been demonstrated to interlink the $(Mo,W)S_4^{2-}$ units. These include Co, Ni, Pb, Cr, and Bi (Bag et al. 2009; Kanatzidis 2011). However, these materials do not have high thermal stability and tend to show measureable mass-loss (~30 mass%) at $T \approx 200°C$ for $NiMoS_4$ (Bag et al. 2009). The mass loss continued to increase with increasing temperature (Bag et al. 2009). However, transition metal substitutions in chalcogels have been demonstrated to improve the thermal stability. Glass formation has not been investigated in this family of materials. It may be possible to sinter or even flux these materials with additional low-melting materials, e.g. sulfur, or low-melting metals, e.g., Sn. A typical preparation includes:

$$MoS_4^{2-} + 0.5\,Ni^{2+} + 0.5\,Co^{2+} \rightarrow Mo\left(Ni_{0.5}Co_{0.5}\right)S_4 \quad (1.3)$$

2.2.2 Search for alternative metals for improved iodine affinity

Historically, various materials were investigated for the capture and immobilization of ^{129}I. In most cases, however, the materials effective for capturing $I_2(g)$ cannot subsequently be sintered and densified to create a mechanically and chemically durable waste form. In the 1970's (Pence et al. 1970; Maeck and Pence 1970; Ackley and Combs 1973; Gal et al. 1974; Pence et al. 1972; Thomas et al. 1977) evaluated metal-exchanged and metal-impregnated materials as potential ^{129}I sorbents. Among these, metal-exchanged mordenite was the most common host material investigated; mordenite is a zeolite with a nominal composition of $(Ca,Na_2,K_2)Al_2Si_{10}O_{24} \cdot 7(H_2O)$, in which the alkali can be exchanged for alternate metals.

In these studies (Pence et al. 1970; Maeck and Pence 1970; Ackley and Combs 1973; Gal et al. 1974; Pence et al. 1972; Thomas et al. 1977), the sodium in the mordenite was replaced with Ag, Cd, Cu, Hg, Mn, Pb, Pd, and Tl, though only Ag proved effective at capturing $I_2(g)$. Thomas et al. (1977) attributed the poor $I_2(g)$ capture efficiency with metals other than silver to the fact that the metal oxides were thermodynamically more stable than the metal iodides. Also worth noting, under a highly reducing atmosphere, Pb-exchanged zeolites showed promise as a secondary adsorbent following the regeneration of the primary Ag-mordenite (Haefner and Tranter 2007).

From the thermodynamic standpoint, when comparing the Gibbs free energy of formation, $\Delta G_f°$, for selected metal oxides at different temperatures (Pankratz 1982) with the corresponding iodide (Pankratz 1984) of same oxidation state, it is evident, for most transition elements, that the oxide is favored over the iodide (Table 1). However, in the case of silver, AgI is thermodynamically favored over Ag_2O (Table 1) at $T \geq 298.15$ K, which is the reason it has been found to be the most effective metal for I_2 removal from air Equations (1.4) and (1.5), where "c", "l", and "g" denote crystal, liquid, and gas, respectively.

$$2Ag(c) + 0.5O_2(g) \rightarrow Ag_2O(c) \; (\Delta G_f° = -11.28 \text{ kJ/mol at } 298.15 \text{ K}) \text{ (Pankratz 1982)} \quad (1.4)$$

$$Ag(c) + 0.5I_2(c,l,g) \rightarrow AgI(c,l) \; (\Delta G_f° = -66.270 \text{ kJ/mol at } 298.15 \text{ K}) \text{ (Pankratz 1984)} \quad (1.5)$$

Table 1 summarizes a few of the $\Delta G_f°$ values for several metal oxides and iodides, including those studied by others for the purpose of removing I_2 from off-gas streams.

2.2.3 Comparison of affinity for competing off-gas components

When considering the high affinity of the chalcogel for I_2, it is not considered a metal-iodide complex, but a chemical affinity that can best be explained with Pearson's Hard/Soft Acid-Base (HSAB) principle (Pearson 1963; Parr and Pearson 1983). The HSAB principle considers the differential complexation behavior of cations and ligands in terms of electron pair-donating Lewis bases and electron pair-accepting Lewis acids (Pearson 1963). Pearson classified Lewis acids and Lewis bases as *hard*, *borderline*, or *soft*. According to Pearson's HSAB principle, hard Lewis acids prefer to bind to hard Lewis bases and weak Lewis acids prefer to bind to weak Lewis bases. Pearson classified a very wide range of atoms, ions, molecules, and molecular ions as hard, borderline or soft Lewis acids or Lewis bases.

In order to explain Pearson's HSAB principle more quantitatively, one can use a parameter called the *chemical hardness*, or η (Parr and Pearson 1983). The chemical hardness is proportional to the second

Table 1. Thermodynamic data comparing the Gibbs free energy of formation ($\Delta G_f°$) for several metal oxides and iodides (Pankratz 1982, 1984). Elements listed in bold were previously studied in metal-exchanged ceramics (Pence et al. 1970; Maeck and Pence 1970; Ackley and Combs 1973; Gal et al. 1974; Pence et al. 1972; Thomas et al. 1977) – note that some do not have listed values.

Temperature, K	Element	Oxide	$\Delta G_f°$, kJ/mol	Iodide	$\Delta G_f°$, kJ/mol
298	**Ag**	Ag_2O	-11.284	AgI	-66.27
	Hg	HgO	-58.551	HgI_2	-102.244
	Ba	BaO	-519.841	BaI_2	-598.078
	Cs	Cs_2O	-308.373	CsI	-340.565
	K	K_2O	-301.273	KI	-323.001
	Pb*	PbO	-187.912	PbI_2	-173.569
	Pb†	PbO	-188.937	PbI_2	-173.569
	Cd	CdO	-228.484	CdI_2	-201.301
	Tl	Tl_2O	-143.482	TlI	-125.47
	Cu	Cu_2O	-147.921	CuI	-69.383
400	**Ag**	Ag_2O	-4.58	AgI	-67.584
	Tl	Tl_2O	-28.1	TlI	-125.738
	Ba	BaO	-151.85	BaI_2	-596.061
	Hg	HgO	-47.58	HgI_2	-100.529
	Cs	Cs_2O	-294.16	CsI	-337.435
	K	K_2O	-287.14	KI	-320.515
	Pb*	PbO	-177.95	PbI_2	-172.322
	Pb†	PbO	-178.74	PbI_2	-172.322
	Cd	CdO	-218.42	CdI_2	-200.033
	Cu	Cu_2O	-140.13	CuI	-69.689

*Massicot (yellow, l)
†Litharge (red, yellow)
‡Minimum

derivative of the total energy of a chemical system (or the first derivative of chemical potential) with respect to changes in the number of electrons in a fixed nuclear environment. The chemical hardness of atoms, molecules, or ions termed species and denoted by the subscript, s, can be calculated from the expression

$$\eta_s = 0.5\left(I_s - A_s\right) \tag{1.6}$$

where I_s is the ionization energy and A_s is the electron affinity of species "s". Since $I_s \geq A_s$, the minimum value of the chemical hardness is zero. With these parameters, one can explain an order of preference for strong adsorption or complex formation between two species. Table 2 presents η values for various Lewis acid and base species "s", or η_s, based on data from the literature (Parr and Pearson 1983; Pearson 1997).

Table 2. Tabulated values of I_s, A_s, χ_s, an η_s for various species, "s", sorted by η_s from hard to soft (Parr and Pearson 1983; Pearson 1997). Competing potential off-gas species are italicized.

Acid/Base	Species	I_s	A_s	χ_s	η_s	Reference
Acid	*HCl*	12.7	-3.3	4.7	8.0	(Pearson 1997)
	HI(g)	10.5	0.0	5.3	5.3	(Pearson 1997)
	HNO_3	11.03	0.57	5.8	5.2	(Pearson 1997)
	I_2(g)	9.3	2.6	6.0	3.4	(Parr and Pearson 1983)
Neutral	*CH_3I*	9.5	0.2	4.9	4.7	(Pearson 1997)
	Cl_2(g)	11.6	2.4	7.0	4.6	(Pearson 1997)
Base	*H_2O*	12.6	-6.4	3.1	9.5	(Pearson 1997)
	S	10.36	2.08	6.22	4.12	(Parr and Pearson 1983)
	Se	9.75	2.02	5.89	3.86	(Parr and Pearson 1983)
	Te	9.01	1.97	5.49	3.52	(Parr and Pearson 1983)

Other species that are present in the off-gas along with I_2(g) as trace contaminants are HCl(g), HI(g), HNO_3, CH_3I, and Cl_2(g). Of these species, HI(g) and HNO_3 can be classified as soft Lewis acids with a chemical hardness comparable to I_2(g) (Table 2) (Pearson 1997). Of the two, HCl is a harder Lewis acid than HI(g) [$\eta_{HCl(g)} = 8.0$]; = 4.7 and = 4.6 though these species are considered neutral according to the HSAB principle (Pearson 1997). Thus, of these other species present in the off-gas stream, HI(g) and HNO_3 could, potentially, compete with I_2(g) for chalcogen binding sites, though the other species will, most likely, not compete according to the HSAB principle. However, since I_2(g) is a weaker Lewis acid than HI(g) and HNO_3, the chalcogen binding affinity for these species is predicted to be I_2(g) > HNO_3 > HI(g) (Table 2).

2.3 Precursor synthesis

2.3.1 K_2MCl_4 and $KMCl_3$ precursors.

The literature (Ohba et al. 1983) suggests that dipotassium tetrachloroplatinate(II) (K_2PtCl_4), a K_2MCl_4-type salt, dissociates in water according to Equation (1.7):

$$K_2PtCl_4 + H_2O \rightarrow 2\,K^+ + \left[PtCl_4\right]^{2-} + H_2O \tag{1.7}$$

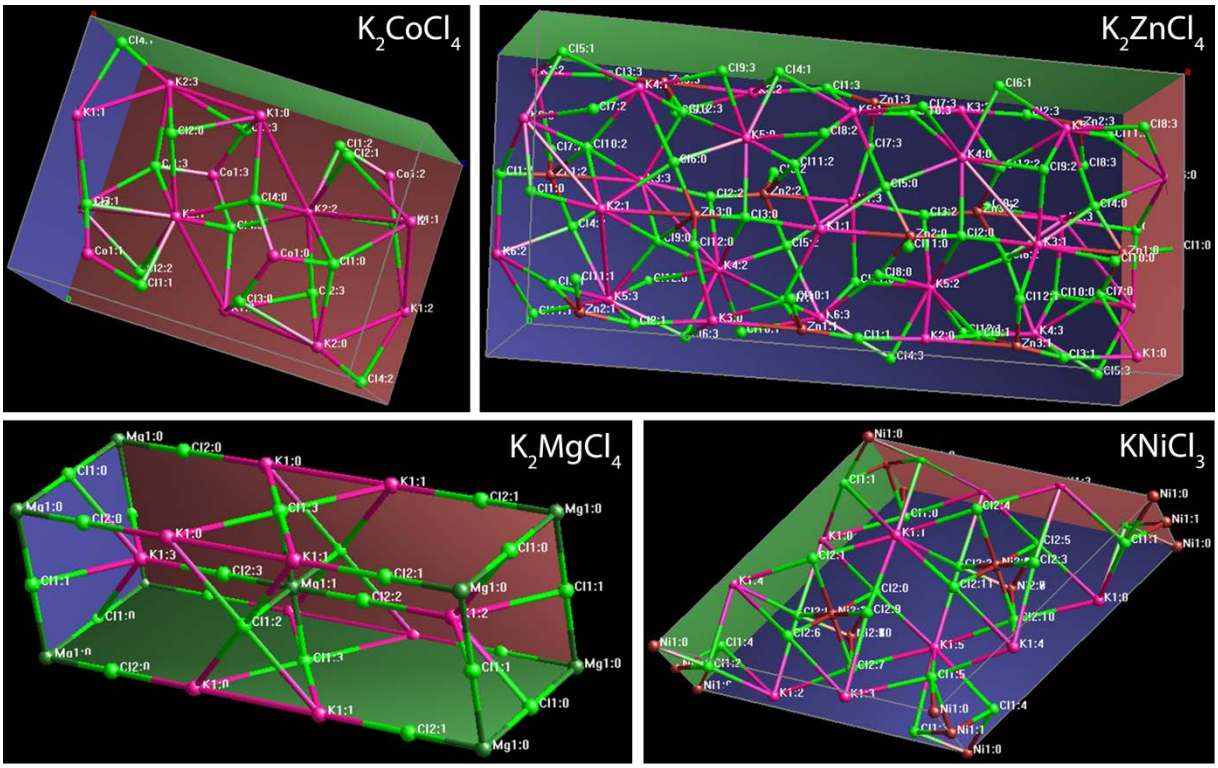

Figure 2. Unit cells for the K_2MCl_4 (M = Co, Zn, and Mg) and $KMCl_3$ ($KNiCl_3$) structures. Structures were exported from Find-It® as .cif files and imported into Topas 4.2. The images above were exported as screen-shots out of the Topas structure viewer. The International Crystal Structure Database (ICSD) numbers for K_2CoCl_4, K_2ZnCl_4, K_2MgCl_4, and $KNiCl_3$ are 661 (Vermin et al. 1976), 80860 (Kusz and Kucharczyk 1995), 4035 (Gibbons et al. 1975), and 10508 (Visser et al. 1980), respectively.

According to Bag et al. (2007), when making a $Pt_2Ge_4S_{10}$ chalcogel, the Pt-Cl bonds of the $[PtCl_4]^{2-}$ anion complex are broken and displaced with Pt-S bonds during the gelation period when making a chalcogel. With this in mind, one of our goals in FY2011 was to extrapolate this concept with precursors devoid of precious metals; that is they contain transition metal alternatives, e.g., Co, Ni, Zn.

The other goal of synthesizing the K_2MCl_4 and $KMCl_3$ precursors was to look at the interlinking ability of differently coordinated metal-chloride species. The approach was to determine the difference in the chemical and physical properties of the chalcogels made with these precursors as the metal ionic species were substituted. As seen in Figure 2, three K_2MCl_4 salts with different coordination were chosen along with a single $KMCl_3$ salt. The coordination of the metals (i.e., Co, Zn, Mg, and Ni) in the following compounds: K_2CoCl_4 (Vermin et al. 1976), K_2ZnCl_4 (Kusz and Kucharczyk 1995), K_2MgCl_4 (Gibbons et al. 1975), and $KNiCl_3$ (Visser et al. 1980) are CN=4, CN=5, CN=6, and CN=6, respectively

These precursor materials were made by combining high purity $MCl_2 \cdot xH_2O$ and KCl salts in separate vials with deionized water, mixing the solutions, and then either heating them or leaving them at room temperature to allow the water to evaporate, leaving behind a 3-component salt. For the $KNiCl_3$ and K_2CoCl_4 materials, the compounds remaining after evaporation were hydrated analogs of the target precursors. In order to remove the water from the compound, the hydrated salts were decomposed by sealing them in fused quartz ampoules and then heating them to >800 °C. See Figure 3 for a brief

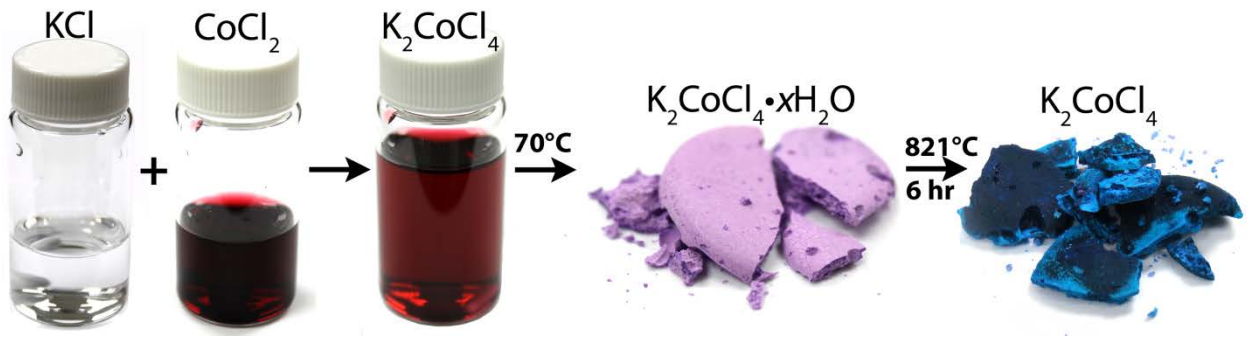

$2KCl\ (H_2O) + CoCl_2\ (H_2O) \rightarrow 2K^+ + Co^{2+} + 4Cl^-\ (H_2O)$ $K_2CoCl_4 \bullet xH_2O$ K_2CoCl_4

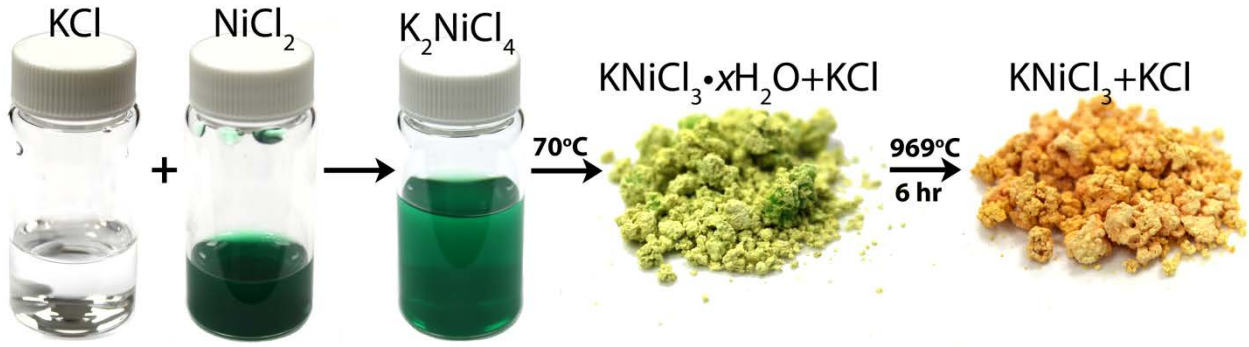

$2KCl\ (H_2O) + NiCl_2\ (H_2O) \rightarrow 2K^+ + Ni^{2+} + 4Cl^-\ (H_2O)$ $KNiCl_3 \bullet xH_2O + KCl$ $KNiCl_3 + KCl$

description of how the K_2CoCl_4 and $KNiCl_3$ were made with the solution-based approach. In FY2012, we will attempt to make chalcogels with these precursors in conjunction with Sn-S precursors.

2.3.2 Sn-S precursors.

One of the Sn-S precursors, $Na_4Sn_2S_6 \cdot 14H_2O$ was fabricated this year. The process was recreated from the methods presented by Oh et al. (2011). Here, 60 mmol of $Na_2S \cdot 9H_2O$ (14.4 g) and 20 mmol of $SnCl_4 \cdot 5H_2O$ (7.01 g) were dissolved in 100 mL of demineralized water and stirred for 24 h yielding a dark green solution. This solution was added, drop-wise, to an Erlenmeyer flask containing 300 mL of acetone while stirring. Upon addition of the Na_2S-$SnCl_4$ solution to the acetone flask, a bluish-white precipitate was observed. This was stirred for 4 h and then placed in a refrigerator for ~72 h. The precipitate, $Na_4Sn_2S_6 \cdot 14H_2O$, was vacuum-filtered with a Büchner funnel, washed with acetone, and dried under vacuum (Figure 4). A similar method can be employed to make $Na_4SnS_4 \cdot 14H_2O$ and $[(CH_3CH_2)_4N]_4Sn_4S_{10}$ (Oh et al. 2011).

Figure 3. Solution-based approach to making K_2CoCl_4 (top) and $KNiCl_3$ (bottom).

Figure 4. Picture of the $Na_4Sn_2S_6 \cdot 14H_2O$ precursor in a 20 mL scintillation vial.

2.4 Chalcogel synthesis

The Mo,W-Co-S_4 hydrogels and W-Co,Ni-S_4 chalcogels were made with techniques described elsewhere (Bag et al. 2009). These materials form very nice hydrogels and can subsequently be made into aerogels with a solvent exchange to liquid CO_2 through ethanol followed by supercritical drying. An example of a W-Co,Ni-S_4 chalcogel made at PNNL is seen in Figure 5. The primary effort in FY2012 will focus on making the gels previously described in section 1.2.1.

Figure 5. Chalcogel #14c [W-Co,Ni-S_4] in a 20 mL scintillation vial.

3. Metal Organic Framework (MOF) Materials

Lead: P. K. Thallapally

Contributors: J. Liu, R. Motkuri, and C. Fernandez

Removal of ^{85}Kr from the process gas streams in a reprocessing facility may be needed to meet 40 CFR 190 requirements. To do this, the current method is to install and operate a cryogenic process. This may be one of four possible processes – cryogenic removal by condensation or condensation on zeolites or silica gel and fluorocarbon absorption. There are variations on each, depending on the institution or country in which they were developed.

A cryogenic distillation process has been successfully used at the ICPP to recover Kr. This is commercial technology, but was not optimized for high Kr recovery decontamination factors. Further development of the cryogenic process has been done in Belgium, France, Germany, and Japan. Decontamination factors of 100 to 1000 have been reported (Goossens et al. 1991). Pilot-scale cryogenic units for krypton recovery in the absence of oxygen have been tested with inactive Kr in simulated off-gas streams at the Kernforshungszentrum (Germany), CEA (France) and SCK·CEN (Belgium) nuclear research centers (Hebel and Cottone 1983; IAEA 1980a). Each unit handles gas flows of 20-50 m^3/h. A radioactive, pilot plant, cryogenic unit for the recovery of ^{85}Kr became active in 1988 in the PNC (now JAEA) facility at Tokai, Japan (Leigh 1994). The system capacity is rated at 110 m^3/h and a ^{85}Kr load of 8000 Ci/d (Naruki 1985). To avoid possible crystallization in the cryogenic distillation column, the Xe is adsorbed on silica gel at -160 °C and 0.3 MPa. A cryogenic system designed to recover ^{85}Kr for beneficial use was operated at the Idaho Chemical Processing Plant for a number of years (Brown et al. 1983; Hebel and Cottone 1982; Bendixsen and German 1975; Goossens et al. 1991; Groenier 1985). The system was designed to treat gases at flow-rates up to 34 - 51 m^3/h (Bendixsen and German 1975).

Fluorocarbon absorption technology was developed at the Oak Ridge Gaseous Diffusion Plant and at the Kernforshungszentrum Karlsruhe (Hebel and Cottone 1982, 1983; Henrich 1985; IAEA 1980b; Little 1983). This process used an organic solvent (CCl_2F_2 called R-12) to selectively absorb noble gases from air or dissolver off gas (DOG) streams; the noble gases are then stripped from the solvent by boiling.

There are several examples in the literature in which zeolites have been tested for Xe/Kr separation. Previous research has shown NaA and NaX zeolite to be selective adsorbents for Xe over Kr with selectivities of approximately four to six (Jameson et al. 1997; Izumi 2003), but with low capacities.

Once separated, the ^{85}Kr-Xe mixture would be stored in steel canisters at moderate pressures. The main problem with this storage method is that the ^{85}Kr decay product is stable Rb. Rubidium has a melting point of 38.9 °C. Only a small amount heating from the decay of ^{85}Kr is needed to heat the canisters to this temperature. Liquid Rb is very corrosive (Pinchback et al. 1981).

Xenon (Xe) and Kr separation is also an industrially important problem. The conventional method to separate these two gases is fractional distillation at cryogenic temperatures, which is an energy-intensive process.

Separation of Xe and Kr from air and from each other by selective adsorption at much higher temperatures, perhaps near room temperature, would be beneficial from two aspects. The process would be more energy efficient, thereby decreasing the operating costs. Additionally, the carbon dioxide from inleaked air and from the fuel would condense on cryogenic units, which requires the removal of CO_2 before removal of the noble gasses. Once separated, the CO_2 would be considered high-level waste due to the ^{14}C content and would require treatment, immobilization and disposal at significant additional cost.

The installation of the process would also be much less expensive; current estimates for the installation of a cryogenic system at a reprocessing plant range up to 20% of the total cost of plant construction.

Since stable Xe would be present in the noble gas inventory of the nuclear fuel and Ar is present in the air, separation of these gases would minimize the volume of noble gas that would need to be immobilized. Under typical plant operations, there would be about 100 times more Ar to be immobilized if not separated and released. There is about 10 times more Xe in the fuel than Kr. Therefore, separating Kr from Xe and from Ar is an important step in removing radioactive ^{85}Kr during treatment of spent nuclear fuel (Kerry 2007). Thus, if a selective adsorbent could be developed with which Ar and Xe could be removed before storage or immobilization, there would be significant savings. Additionally, if these adsorbents could reduce ^{85}Kr concentrations in the Xe-rich product to permissible levels, there could be an entirely new industrial supply of Xe. There is a strong incentive to develop novel adsorbents for the removal of ^{85}Kr from process gases in a reprocessing plant.

Different from zeolites, metal-organic frameworks (MOFs) represent a new class of functional materials consisting of metal centers linked with organic building blocks to produce diverse and customizable structural frameworks. These metal centers and organic linkers readily self-assemble into materials with open framework structures, where all the porosity is accessible for gas storage, separation, and catalysis (Férey et al. 2011; Lee et al. 2009; Li et al. 2009). MOFs have received considerable attention over the past few years because of their high surface areas, large and tailorable pores, and adjustable chemical functionalities (Li et al. 1999; Rowsell et al. 2005; Thallapally et al. 2008).

Although research to date is somewhat limited with regard to the noble gases, storage and separation of noble gases has been demonstrated with some MOFs. A porous MOF-filled container stores substantially more Xe or Kr than the same container without any sorbent as shown in compression curves of Figure 6 (Mueller et al. 2006). For the Cu-MOF studied, the capacity for Xe was twice that of a high surface area carbon (Ceca, AC-40, 2000 m^2/g). In addition, properties for separating Xe and Kr have been demonstrated. The gas diffusion in a MOF is 2-3 orders of magnitude higher than in high performance carbons and molecular sieves (Mueller et al. 2006). This should lead to superior performance with greater speed and reduced energy consumption in technological applications. It is also possible to increase the uptake of Kr and Xe with high surface area materials that have been reported (Bourrelly et al. 2005).

These materials could augment the existing technology for the removal and storage of Kr. One of the main concerns with storage of cryogenically separated Kr in stainless steel canisters at elevated pressures (the baseline approach) is the Rb that is formed as the ^{85}Kr decays. The use of MOFs augments this technology in two ways. First, it allows more gas to be stored in the canister (Figure 6) at lower pressures. Secondly, the decay product Rb would be isolated from the metal canister, since it would be in the MOF structure, thereby reducing the corrosion concerns.

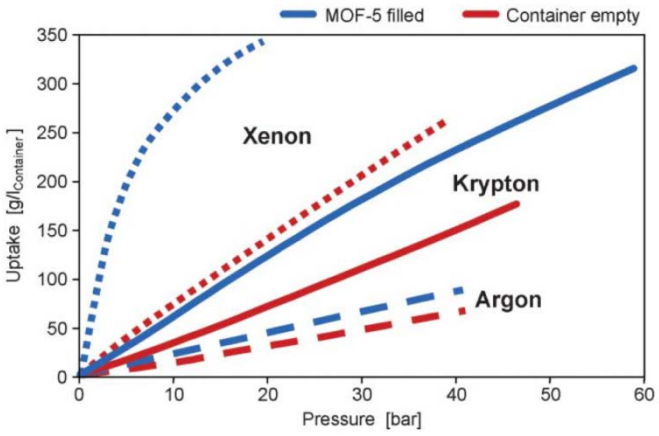

Figure 6. Enhanced noble gas storage capacities for cylinders filled with MOF-5.

Because the chemical properties of Kr and Xe are very similar, it is likely that any process to remove Kr is likely to also remove Xe, since it is heavier and more reactive. Of these two elements, fission product Xe is much more

abundant and all of the radioactive Xe isotopes are very short lived (half-life ≤ 36 d). So the radioactive Xe isotopes will have decayed to insignificant amounts by the time the fuel is processed. However, ^{85}Kr has a 10.7-y half- life. In the cryogenic process, Xe and Kr are removed together with further separation difficult. This complicates the storage and potential immobilization challenge, since there is about 15 times more Xe than Kr. It would be beneficial to find a novel MOF that has high Xe and Kr capacities at relatively high temperatures in order to separate and store them, but better yet if there is sufficient specificity that the two could be separated from each other.

The goal of this study is to design, synthesize, and test novel MOF materials that they have the desired Xe and Kr adsorption properties, i.e., high capacities, selectivities, and easy to engineer process temperature and pressure.

3.1 Experiment and apparatus

3.1.1 Material synthesis

Generally, MOFs are synthesized through hydrothermal or solvothermal reactions. For example, Ni/ 2,5-dihydroxybenzenedicarboxylic acid (DOBDC) is synthesized following a solvothermal reaction procedure (Dietzel et al. 2009). A solution of 2,5 dihydroxyterephthalic acid (1.486 g, 7.5 mmol) in tetrahydrofuran (THF) (25 mL) and a solution of nickel(II) acetate tetrahydrate (3.733 g, 15 mmol) in water (25 mL) are combined in a Teflon®-lined vessel. This is placed into an autoclave, which is then sealed. The contents are allowed to react for 3 days at 383 K. Filtration of the resulting mixture yields 3.107 g of a yellowish, fine crystalline product that is then washed three times with water. Powder X-ray diffraction confirms the identity of the compound.

From the resulting very fine powder, coarser material is formed in a two-step process. First, the fine powder is pressed into a pellet under 850 MPa for 5 min. Secondly, the resulting pellet is broken and coarsely seived to obtain a 600-850 μm powder.

3.1.2 Apparatus and procedure

Static adsorption experiments with pure Kr and Xe were performed with an automated gas sorption analyzer Quantachrome Autosorb IQ (Figure 7). A water bath was used to maintain 25°C.

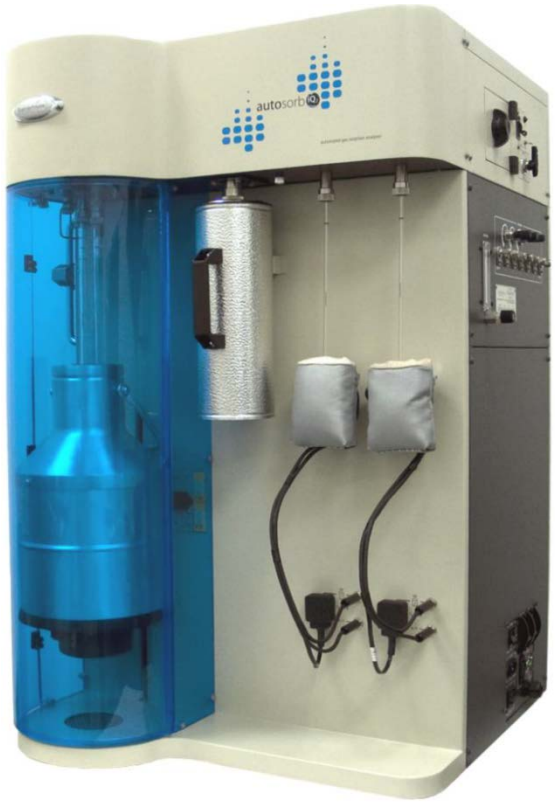

Figure 7. Quantachrome Autosorb IQ for static pure Xe and Kr adsorption measurement.

An intelligent gravimetric analyzer (IGA; Hiden Analytical Ltd., Warrington, UK) was used to perform the Xe/Kr mixture breakthrough measurements. The IGA system has a dynamic sorption analyzer (shown schematically in Figure 8) that can handle breakthrough adsorption experiments for multiple components (Lillo-Ródenas et al. 2006).

Powdered samples were packed as a fixed adsorption bed for the breakthrough experiments. The dynamic sorption analyzer was used to measure Xe/Kr break-through. Gases are introduced through the bottom inlet of the adsorption bed and MOF powders were held between two layers of quartz wool and two

sample holders. Frit gaskets were installed at the top and bottom of the adsorption bed to prevent powder contamination of the main gas line.

The samples were regenerated in-situ by heating overnight at certain temperatures under a helium purge. Before regeneration, the gas line was purged with a gas mixture that is the same as that to be used in the test; the flow-rate is the same as that to be used in the test. Dead volume and delay times in the mass spectrometer signal were determined and used to correct the measured breakthrough capacity. Activated sample mass was determined immediately after unloading the sample and the ideal gas law was used to calculate the moles of gas adsorbed by MOF samples.

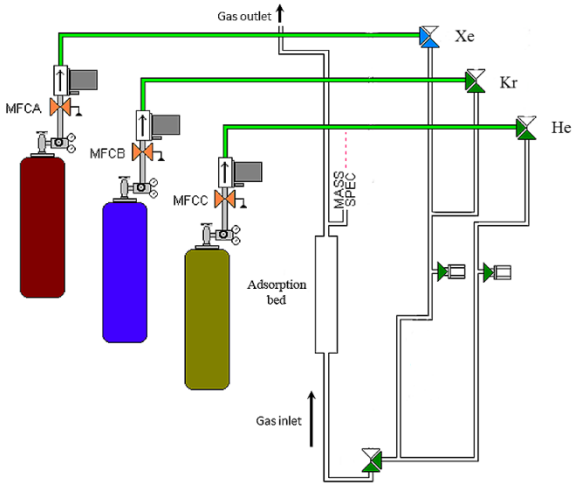

Figure 8. Apparatus for the Xe/Kr breakthrough experiments.

3.2 Xe/Kr adsorption in MOFs

3.2.1 MOF Ni/DOBDC

3.2.1.1 Pure Xe and Kr adsorption

In order to compare with the pure Xe and Kr adsorption isotherm data obtained by using the static method (IGA, gravimetric method), pure Xe and Kr breakthrough measurements were made before the Xe/Kr mixture experiment. The pure Xe and Kr room temperature isotherms obtained through static method are shown in Figure 9. Results for a benchmark adsorbent activated carbon are also included for comparison. The Ni/DOBDC has a little bit higher Xe capacity (55 mass%, 4.16 mol/kg) and lower Kr capacity (8 mass%, 0.95 mol/kg) than the activated carbon at about 100 kPa. Pure Xe capacity at 100 kPa determined by breakthrough curves is close to that obtained through static method for the Ni/DOBDC sample (static Xe capacity: 4.16 mol/kg at 100 kPa; Breakthrough Xe capacity: 3.83 mol/kg at 100 kPa). This result indicates that Ni/DOBDC has a high Xe capacity and may have a higher Xe/Kr selectivity than that of the activated carbon. Therefore, it is promising to use Ni/DOBDC to separate and store Xe from the spent nuclear fuel.

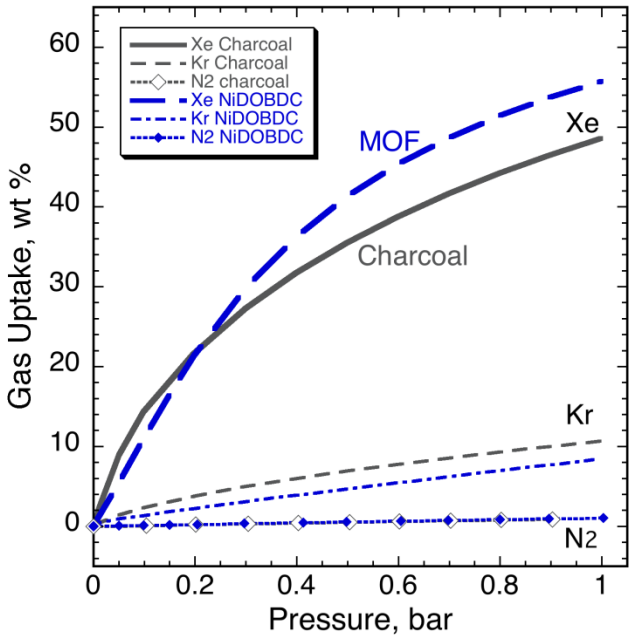

Figure 9. The 25 ^{o}C Xe, Kr, and N_2 isotherms for Ni/DOBDC and an activated carbon.

3.2.1.2 50:50 Kr/Xe breakthrough

Before breakthrough experiments, the Ni/DOBDC sample was regenerated at 250 °C under a helium purge for 15 h initially and 3h for the subsequent experiments. The breakthrough experiments were conducted at 25 °C and the total gas flow rate was 50 mL/min at 100 kPa. Three Kr/Xe mixtures (20 mass%/80 mass%; 50/50; 80/20) were studied. Results from the 80/20 case are shown in Figure 10 as an example.

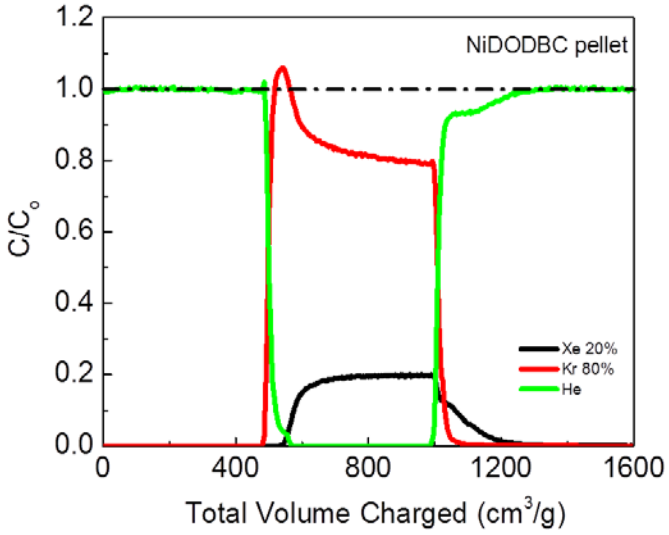

Figure 10. The 25 °C Kr/Xe (80:20) breakthrough curves for the Ni/DOBDC.

It is obvious that Ni/DOBDC has a higher specificity for Xe than Kr at room temperature. It takes some time for Xe to breakthrough, while Kr broke through the adsorption bed almost immediately. The Xe and Kr selectivities and capacities at different gas ratios for the Ni/DOBDC sample are summarized in Figure 9.

The Xe/Kr selectivity for the Ni/DOBDC sample decreases from 4 to 2.3 when the concentration of Xe in the mixture increases from 20% to 80%. Compared to simulation work reported in the literature (Ryan et al. 2011), it seems that our Ni/DOBDC has similar Xe/Kr selectivity to IRMOF-1 [Zn_4O(H-1,4-benzenedicarboxylate)$_3$] and UMCM-1[University of Michigan Crystalline Material; Zn_4O(Benzene-dicarboxyllic acid)(tris(4-carboxyphenyl)-benzene)$_{4/3}$], but a lower Xe/Kr selectivity than HKUST-1[Cu_3(1,3,5-benzene-tricarboxylic acid)$_2$] , MOF-505, and several other MOFs with a total pressure of Xe and Kr at 1 bar. However, from other reported simulation work, Xe/Kr selectivity for IRMOF-1 showed that IRMOF-1 has only a Xe/Kr selectivity of 2.5 with 10% Xe and 90% Kr in the mixture at 1 bar (Greathouse et al. 2010). Moreover, notice that the selectivity we obtained here is an overall selectivity that is the product of the equilibrium selectivity and the kinetic selectivity. Since Kr diffuses faster into pores than Xe, the overall Xe/Kr selectivity is dictated by slower diffusion rate of Xe. Therefore, it is important to study the Xe/Kr selective adsorption through experiment besides simulation, in which usually only the equilibrium selectivity is considered. If only theoretical results are considered, important materials might be overlooked.

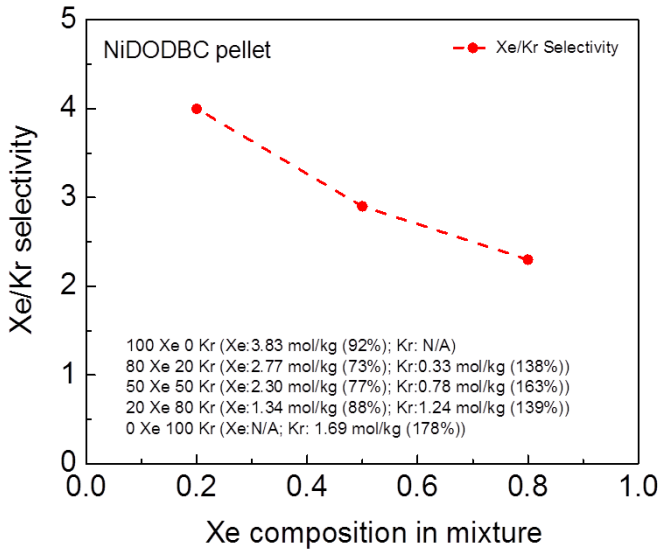

Figure 11. The Xe/Kr selectivities at different ratios of Xe/Kr mixture at 100 kPa and 25 °C for the Ni/DOBDC.

The capacities, in mass% gained relative to

the original mass, are obtained from breakthrough measurements rather than results from static methods for both Kr and Xe. These results are shown in the parentheses in the legend entries of Figure 11. The percentages for Xe decrease with increasing Xe concentration and may be caused by possible competitive adsorption of Kr in the Ni/DOBDC.

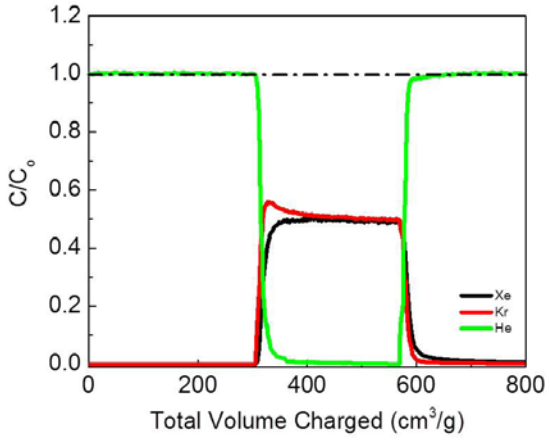

Figure 12. The Xe/Kr (50:50) breakthrough curves at 25 °C for the proprietary MOF.

3.3 New MOFs

3.3.1 A new MOF

Besides the well-known MOFs, such as Ni/DOBDC, we also developed and synthesized new MOFs and investigated their application to remove and immobilize Kr and Xe. Recently, we developed a new MOF specifically for the separation of Kr from Xe and air at near room temperature. We are determining the specificity for Xe and Kr in this new MOF and initial results are encouraging. Because this new MOF is proprietary, no details about the preparation or composition of this MOF are discussed here.

The Xe/Kr (50:50) breakthrough curves for the new MOF are shown in Figure 12. The Xe capacity was calculated to be 0.51 mol/kg and the Kr capacity was calculated to be 0.32 mol/kg. Therefore, the selectivity of Xe over Kr for the new MOF under our current experimental conditions is 1.6, which indicates that the new MOF has equal selectively for Xe and Kr at room temperature within experimental error.

3.3.2 MOF PNNL-5DB

Another new MOF, PNNL-5DB, was obtained by starting with $Zn(NO_3)_2 \cdot 6H_2O$ and the general procedure shown in Section 3.1.1 The resulting solution was stirred for 1 h at room temperature, and then a white precipitate was filtered off. The resulting solution, upon heating to 95 °C for 7 h, produced colorless, brick-shaped crystals. The product (105 mg) was washed with dimethylformamide and methanol. Crystallographic measurements of the resulting crystals show that the solvent-accessible voids in the crystal are estimated to account for 55% of the crystal volume, with the simultaneous occupation of all disordered sites of dabco ligands. The dicarboxylate linker in the crystal structure of PNNL-5DB is conformationally ordered, and the dihedral angle between the phenyl ring and carboxylate plane is 44.4°. The material was activated by heating at 150 °C for 12 h under vacuum.

The PNNL-5DB MOF was characterized with thermogravimetric analysis coupled to mass spectrometry (TG-MS) and powder X-ray diffraction (pXRD). In addition, Kr as well as Xe

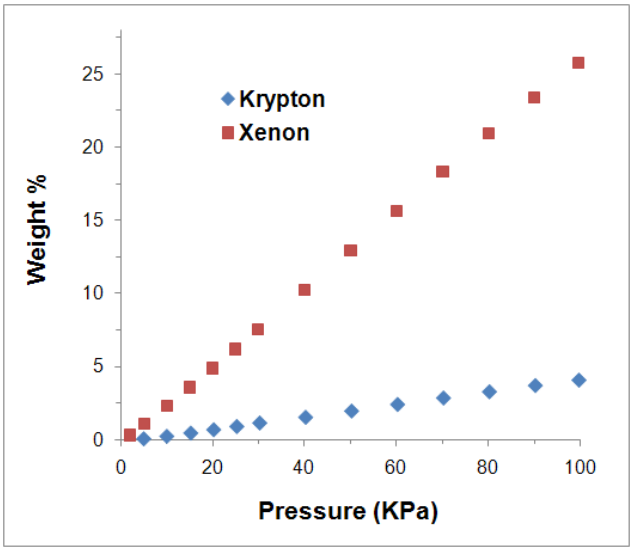

Figure 13. The 25 °C isotherms on Kr and Xe for the PNNL-5DB MOF.

adsorption/desorption experiments at room temperature were performed. These characterization analyses were carried out in order to verify the identity of the sorbent materials, to determine the sorption capacities for each noble gas, and to understand the sorbent stability after an adsorption-desorption cycle. The TG-MS analysis indicated a mass loss of 19% for the PNNL-5DB prior to its thermal decomposition. This mass loss is mainly due to the removal of solvent molecules. Based on this information the sorbent was evacuated for several hours prior to adsorption measurements.

For adsorption studies, the sample was placed in a fixed-volume glass container and the temperature of the Quantachrome furnace was increased to 150 °C under vacuum at a rate of 5 °C/min. The sample was then activated at that temperature for 12 h prior to uptake measurements. The dry mass of the adsorbent was determined and the experimental temperature (25 °C) was maintained with a programmable water bath. The sample compartment was then pressurized at fixed initial pressures and allowed to equilibrate to constant pressure at each sorption equilibrium step. The adsorption analyses were carried out at 14 pressures over the range between 0.1 and 100 kPa. Each pressure point was set and maintained through the opening/closing of inlet/outlet valves via computer control. After equilibrium was established at a given pressure, a mass measurement was made and the gas pressure increased to the next set pressure value. The gas pressure drop (related to gas volume decrease) due to adsorption for each pressure step was plotted against the pressure and the gas uptake at each pressure can be calculated based on the initial (dry) sample weight. Figure 14 shows the isotherms obtained for Kr and Xe at 25 ºC. At 100 kPa and 25 ºC Kr capacity is 4.1 mass%. The sorption capacity of Xe was larger at 25.7 mass%.

3.3.3 MOF PNNL-Mn

The last new MOF we developed during this period is the PNNL-Mn. We adapted a pillaring idea from the literature and tried to synthesize 3-D MOFs from their 2-D precursors with pillaring ligands (Kitaura et al. 2004). This strategy has already been successfully used in inorganic compounds, resulting in many pillared layer porous materials being synthesized, such as pillared montmorillonite and smectite (Ohtsuka 1997). However, the number of MOFs designed by use of this strategy is still rare in the literature.

Here, we report the synthesis of a 3-D Mn-bearing MOF by insertion of a pillaring agent. This pillar insertion reaction involves a sliding of the 2-D layers, resulting in a considerable increase in the channel size and pore volume dimensions. The PNNL-Mn was prepared in a heterogeneous reaction at 373 K in a stainless reaction vessel for 18h.

The single crystal structure of PNNL-Mn will be determined in the near future. According to the literature, this type of material is a 3-D open framework composed of two-dimensional grid layers constructed by the Mn (II) ions and the organic groups, including the pillaring agent (Kitaura et al. 2004). This framework is stable and retains its original structure after removing the solvents.

Powder XRD pattern is shown in Figure 14. It is clear that the PNNL-Mn has good crystallinity. The BET surface area for the PNNL-Mn was calculated to be 374.76 m^2/g based on its 77K N_2 isotherm in Figure 15. The isotherm is a type I isotherm and there is no hysteresis in the isotherm which indicates that the PNNL-Mn is a microporous material.

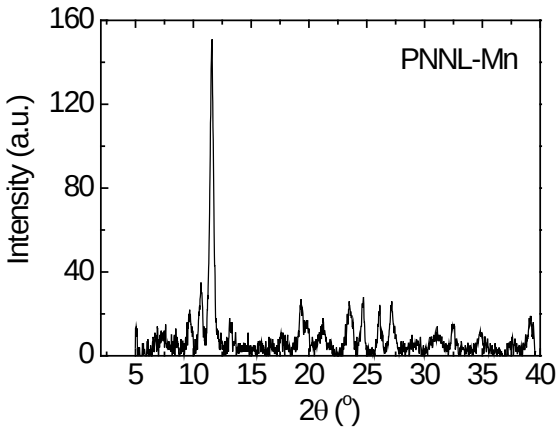

Figure 14. The XRD pattern for the PNNL-Mn.

Krypton and Xe adsorption in PNNL-Mn at room temperature has been studied. The sample was activated at 150 °C for 12 h previous to analysis. The net mass of the activated sample was determined and the experimental temperature (25 °C) was maintained with a programmable water bath. In addition, the whole system was evacuated before introducing Kr or Xe. The sample compartment was then pressurized at different pressures and equilibrium was recorded when no pressure variation was detected. The Kr and Xe isotherms for PNNL-Mn at room temperature are shown in Figure 16.

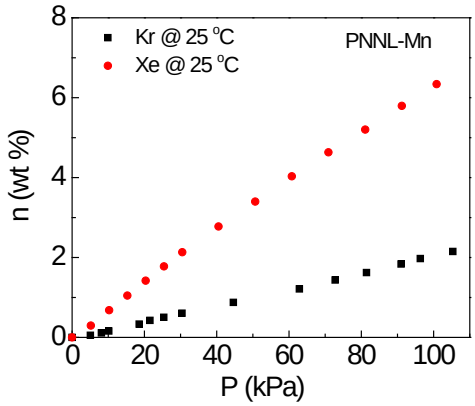

Figure 15. The 25 °C Kr and Xe isotherms for the PNNL-Mn.

It is clear that the PNNL-Mn adsorbs more Xe than Kr at room temperature. It has comparable capacities for Xe and Kr as MOF-5 (IRMOF-1) reported in the literature (Mueller et al. 2006) . Considering the density of PNNL-Mn is greater than that of MOF-5, PNNL-Mn can adsorb more Xe and Kr than MOF-5 given a container of the same volume. Therefore, a cylinder loaded with PNNL-Mn can adsorb much more Xe and Kr than an empty cylinder under the same conditions. The next step is trying to study the surface hydrophobicity of PNNL-Mn and whether the PNNL-Mn can adsorb significant Kr from air

3.4 Conclusions and Path Forward

The Ni/DOBDC has higher Xe capacity than the benchmark activated carbon and Ni/DOBDC can selectively adsorb Xe over Kr. The Xe/Kr selectivity of the Ni/DOBDC decreases as the concentration of Xe in the mixtures increases. It is important to study both the equilibrium and the kinetic selectivity of Xe/Kr for practical applications.

An interesting new MOF was developed. This new MOF selectively adsorbs Xe over Kr at room temperature, but it has the potential to reverse the selectivity at different temperatures. We are awaiting further positive developments before filing a patent disclosure on this MOF.

We have synthesized two other MOFs that selectively adsorb Xe over Kr at room temperature. The two new MOFs have hydrophobic surfaces that are expected to minimize water effects on Xe and Kr adsorption.

The next step is to study Kr and Xe adsorption from air. The final target is trying to develop a MOF that can immobilize both Xe and Kr and selectively adsorb Kr over Xe. In the near future, the effects of water in the gas stream on Kr and Xe adsorption in MOFs will be studied.

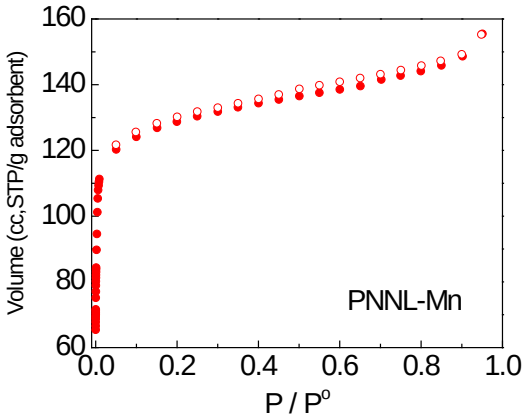

Figure 16. The N_2 isotherm at 77 K for the PNNL-Mn.

4. Silver-functionalized silica aerogels for capture and immobilization of gaseous radioiodine from reprocessing off-gas

Lead: J Matyáš

Contributors: G. E. Fryxell, B. J. Busche, and M. J. Robinson

4.1 Summary

Silver-functionalized silica aerogels developed at Pacific Northwest National Laboratory (PNNL) shows great promise in effective removal and immobilization of gaseous iodine that is released during reprocessing of spent nuclear fuel. The developed material exhibits decontamination factors (DFs) in excess of 10^4 with maximum iodine sorption capacity of 47.6 mass% which is more than 4 times higher than that of the reduced silver mordenite (11.1 mass%). In addition, the sintering tests with raw silica aerogel granules indicated that the iodine-loaded aerogel can be consolidated to form a dense and durable waste form with little loss of I_2 at temperatures between 1050 and 1200 °C where rapid densification was observed.

4.2 Iodine sorption performance

Following is a description of the tests performed at PNNL and Oak Ridge National Lab (ORNL) to determine the DF and maximum iodine sorption capacity for Ag-functionalized silica aerogels.

4.2.1 Breakthrough test at PNNL

The silver-loaded silica aerogels containing an estimated 30 mass% Ag were tested for I_2 uptake from breathing air containing I_2 4.2 ppmv and H_2O at 67 ppmv. Figure 17 shows a schematic diagram of the experimental apparatus. Air was allowed to pass through an U-tube containing glass beads and an I_2 permeation tube. The I_2 concentration of 44 mg/m^3 in the carrier gas was established by heating the permeation tube in the oven to 100 °C and adjusting the carrier gas flow rate to 18.9 mL/min (linear velocity 401 mm/s). The air with I_2 was allowed to pass through the column with 737 mg of reduced-Ag aerogel at150 °C to an I_2 trap containing 20 mL of 0.1 M NaOH; this was replaced at various times. The collected solutions were analyzed for I_2 with inductively coupled plasma-mass spectrometry (ICP-MS) with detection limit for I_2 4 µg/L.

No I_2 breakthrough was observed up to 26 days, indicating DFs in excess of 10^4. Figure 18 shows the change in DF over the time. Initial low DF values are probably due to contamination of 0.1M NaOH solutions by residual iodide from caustic solutions used for calibration.

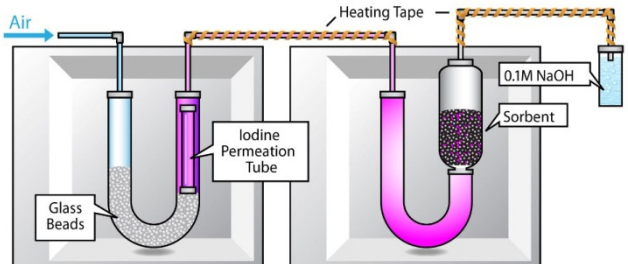

Figure 17. Schematic Diagram of the Experimental Set-up for Iodine Uptake Test in Breathing Air Containing I_2 at 4.2 ppm.

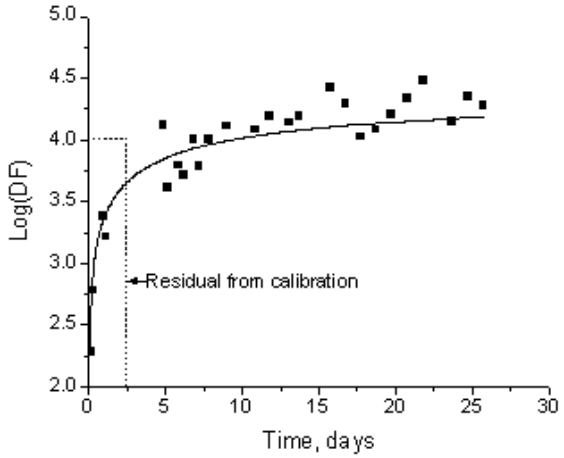

Figure 18. Decontamination Factor over Time for Ag-Functionalized Silica Aerogel.

4.2.2 Maximum sorption test at ORNL

A large capacity thermal gravimetric analyzer (TGA) at Oak Ridge National Lab (ORNL) was used to study the interaction of I_2 with granules of Ag-loaded silica aerogel and to determine the maximum sorption capacity. The schematic of this apparatus is shown in Figure 19. The TGA apparatus was assembled with a modified VWR model 1330GM standard laboratory oven, a Mettler-Toledo Model XS603S balance, a three-legged weighing pan that holds the sample in a wire-bottom basket, and a gas mixing manifold with flow controllers and an iodine column. Surrounding the weighing pan that extends out of the oven heat zone to the microbalance below was a glass cylinder with an open top.

The air stream with the iodine concentration of 400 mg/m^3 and superficial velocity of 10 m/min was generated in the gas mixing manifold by mixing the I_2 saturated stream with dry air. The total flow rate during the test was 11.86 L/min. The I_2 saturated stream was produced by purging air stream through a column of iodine crystals under the controlled flow and temperature conditions. The iodine concentration in the air stream was verified analytically over the specific time interval before and after a run by reaction with NaOH. The oven temperature was maintained at 150°C and standard atmospheric pressure 101.3 kPa.

The granules of Ag-functionalized silica aerogel were loaded into the wire basket and dried for 12.5 h in dry N_2 at 2 L/min until no change in apparent mass was observed, the aerogel starting mass (m_{start}) 1.360 g. Then, the air stream with the I_2 was passed through a 6-m Teflon® tube heat exchanger before entering the glass cylinder. The glass cylinder simulated what a "slice" from a deep bed of iodine sorbent material would experience in a packed bed column. The increase in sample mass was recorded every minute, displayed

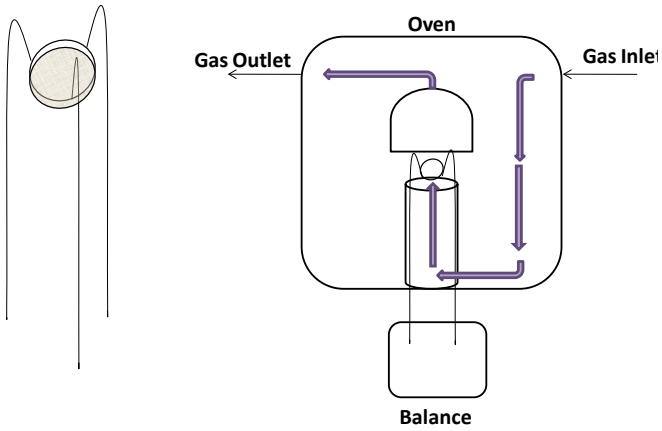

Figure 19. Simple Schematic of TGA Apparatus.

real-time in an Excel spreadsheet, and simultaneously plotted on an Excel chart display.

Figure 20 shows the iodine sorption performance of aerogel granules over the time. After 87 h, the sample mass had reached 1.990 g, corresponding to a 46 mass% increase. Then, the sample was purged for 25 h with an air stream at the same total flow rate to determine the amount of physically sorbed I_2. Since no apparent mass loss or gain was observed the test was continued for an additional 98 h. The apparent sample mass increased from 1.990 g to 2.016 g. As before, the sample was purged with air for 65 h. The final apparent mass of the sample was 2.007 g for an iodine loading 47.6 mass%, which indicated a very small amount of physically adsorbed iodine on the sample surface (0.009 g or 0.4 relative %). Figure 21 shows the appearance of granules before (black) and after (brown) the test.

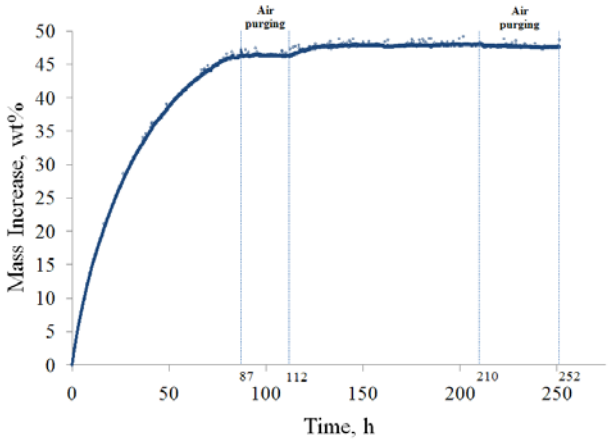

Figure 20. The Increase in Mass of the Ag-functionalized Silica Aerogel during the Test at ORNL.

4.2.3 Densification behavior of silica aerogels

The iodine-loaded aerogel can be consolidated to form a dense and durable waste form with little loss of I_2 at temperatures above 900°C. To determine the optimum densification conditions, the sintering behavior of silica aerogel granules during isothermal heat treatments at temperatures from 900 to 1400°C and times from 2.5 to 90 min was investigated. The Brunauer, Emmett, Teller (BET) surface areas were determined as were the densities with helium pycnometry.

Figure 21. Silver-functionalized Silica Aerogel before (left) and after (right) Maximum Sorption Test.

Table 3 shows the skeletal density, surface area, total pore volume, and average pore size for adsorption and desorption for as-received trimethylsilylated (hydrophobic) silica aerogel granules. The size of irregularly shaped and translucent granules varied from 1 to 4 mm. The low skeletal density of granules compared to bulk density of amorphous silica (~ 2.2×10^3 kg/m^3) comes from the lower density

Table 3. Physical Properties of As-received Silica Aerogel Granules.

Skeletal density, 10^3 kg/m^3	Surface area, m^2/g	Total pore volume, $\times 10^{-3}$ m^3/kg	Average pore size (Ads/Des), nm
1.7	1114	7.41	18.7/6.5

trimethylsilylated groups, closed pores, and complex nature of micropore structure. It is difficult to completely fill the pores even when the porosity is entirely open. The measured high surface area of 1114 m^2/g, large total pore volume of 7.4×10^{-3} m^3/kg and majority of pores in the mesopores regime, those with diameters between 2 and 50 nm, is typical for silica aerogels.

For each sample, about 60 mg of granules were evenly distributed inside of the Pt-boats and isothermally heat-treated in the furnace at 900, 1050, 1200, 1300, and 1400°C for 2.5, 5, 15, 25, 40, 60, and 90 min. Then, the granules were allowed to cool to room temperature in a vacuum desiccator and were removed just before analysis to minimize contamination.

Figure 22 shows the evaluation of skeletal densities for raw granules after heat-treatments at different temperatures for various times. Densities of more than 2.1×10^3 kg/m^3 were attained in less than 2.5 min at temperatures from 900 to 1300°C, suggesting that the densification process occurs very fast. For granules heat-treated at 1050 and 1200°C, the densities ranged from 2.1 to 2.3×10^3 kg/m^3. Samples heat-treated at 1300°C reached a minimum of 1.1×10^3 kg/m^3 after 25 min; samples heat-treated at 1400°C reached a minimum of 1.4×10^3 kg/m^3 after 5 min. With extended heating at 1300°C for 706 min and at 1400°C for 60 min the density increased to 2.1×10^3 kg/m^3. The initial low density values at 1400°C and significant decrease of density over the time for granules heat-treated at 1300°C were caused by foaming. Figure 23 shows three sizes of aerogel granules - < 0.84 mm, 0.84 – 2 mm, >2 mm - after 2.5 min at 1400°C. Different size granules responded similarly to this heat-treatment. They got smaller, became opaque, and had lots of tiny bubbles in them.

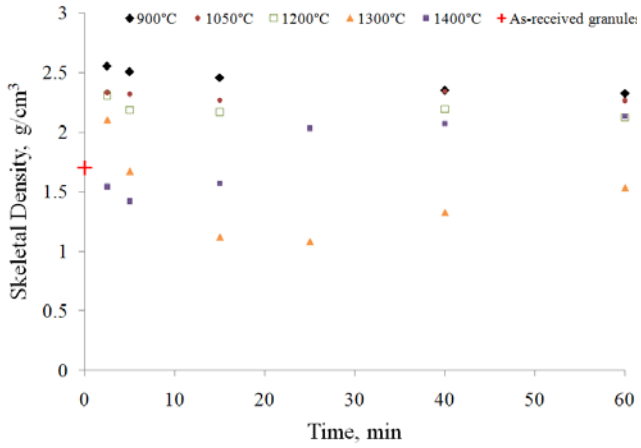

Figure 22. Change of Skeletal Density over the Time and Temperature for As-received Silica Aerogel Granules.

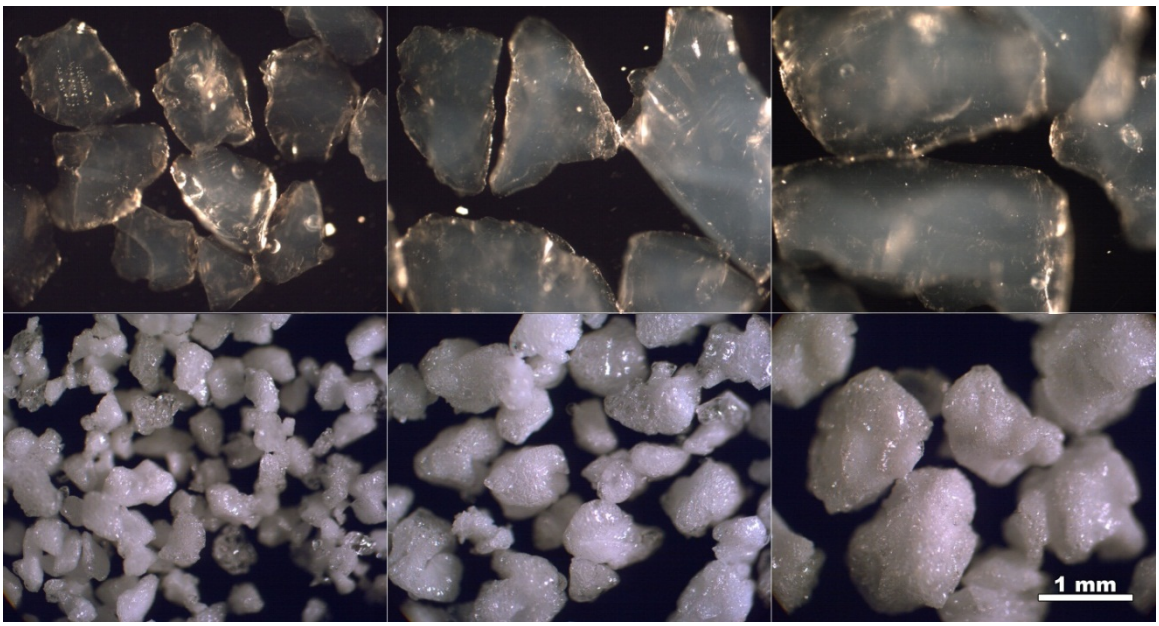

Figure 23. As-received Silica Aerogel Granules before (top row) and after Heat-treatment at 1400°C for 2.5 min (bottom row). From Left to Right Column Granules Size Varies from < 0.84 mm, 0.84 – 2 mm, to > 2 mm.

Table 4. Changes in the Surface Area, Total Pore Volume, and Average Pore Size for Adsorption and Desorption for Samples Heat-treated at 900, 1050, and 1200°C for Different Times

Temp., °C	Time, min	Surface area, m^2/g	Total pore volume, 10^{-3} m^3/kg	Average pore size (Ads/Des), nm
900	2.5	1051	7.73	33.5/23.9
900	5	946	6.57	32.0/17.8
900	15	987	6.77	32.5/24.7
900	60	909	6.08	32.0/19.2
1050	2.5	724	3.58	24.0/18.6
1050	5	482	2.33	23.1/15.7
1050	15	466	1.96	23.9/15.5
1050	40	464	1.91	24.0/15.5
1050	60	348	1.3	18.7/13.1
1200	2.5	397	1.45	18.7/12.6
1200	5	68	0.23	10.3/6.8
1200	15	25	0.09	7.5/7.4

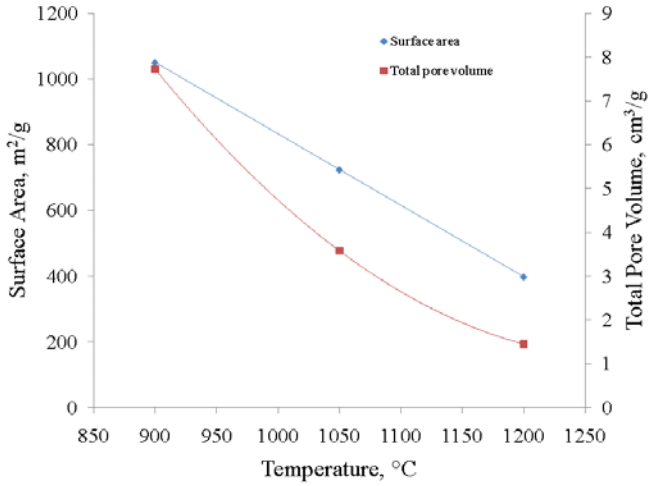

Figure 24. Change of Surface Area and Total Pore Volume for As-received Silica Aerogel Granules after 2.5-min Heat-treatments at 900, 1050, and 1200 °C.

Desorption for Samples Heat-treated at 900, 1050, and 1200 °C for Different Times. Table 4 shows the impact of temperature and time on the surface area, total pore volume, and average pore size for as-received silica aerogel granules. At 900 °C, only small changes in the surface area, total pore volume, and average pore size were observed. At 1050 °C, the surface area decreased by more than 35, 56, and 68% after 2.5, 5, and 60 min, respectively. The total pore volume decreased as well, from 7.41×10^{-3} m^3/kg to 1.3×10^{-3} m^3/kg after 60 min. As expected, the densification process was even faster at 1200 °C. After 15 min at this temperature the surface area of granules decreased by more than 97% to 25 m^2/g, total pore volume by more than 98% to 9×10^{-5} m^3/kg, and average pore size by more than 59% to 7.5 nm. The impact of 2.5-min heat-treatments at 900, 1050, and 1200 °C on the surface area and total pore volume is visualized in the Figure 24 and the progress of densification for short heat-treatments (2.5, 5, and 15 min) at 1200 °C is demonstrated in the Figure 25. The results from densification experiments indicated that the optimum densification temperature for iodine-loaded aerogel lies between 1050 and 1200 °C where rapid densification was observed.

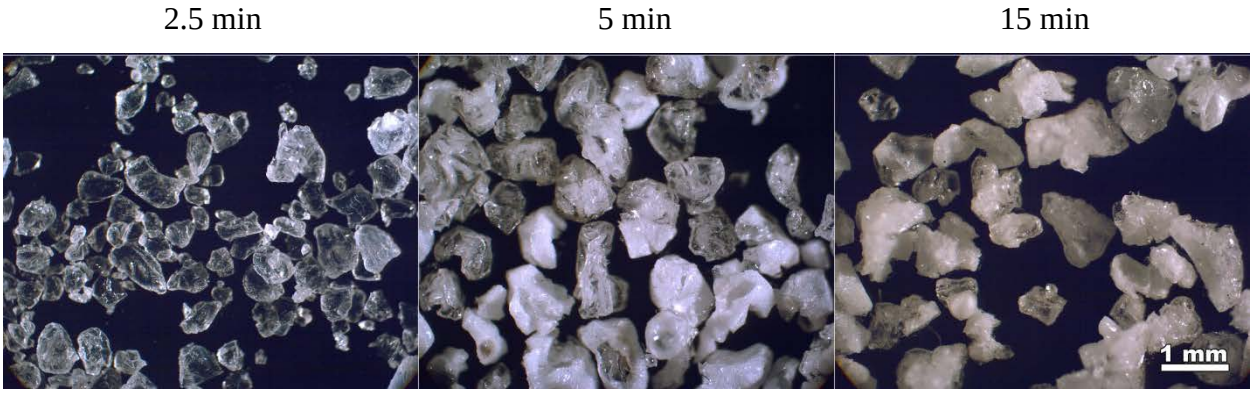

Figure 25. Appearance of Silica Aerogel Granules after 2.5, 5, and 15 min at 1200 °C

5. Immobilization of ^{85}Kr in Silicon Carbide

Lead: J. V. Ryan

Contributors: W. Bennett, C. C. Bonham, and V. Shutthanandan

5.1 Background

Although the half-life for ^{85}Kr is only 10.7y, there are safety concerns and high storage volumes associated with storage of Kr in pressurized gas cylinders. Therefore, a solid SiC immobilization form is being investigated. The method of immobilization in SiC lends itself easily to the immobilization of other elements at the same time as SiC is being laid down including both ^{14}C and ^{129}I which have significantly longer half-lives and require immobilization for many half-lives.

Because of the low diffusivities for gasses and the superior physical and chemical stability of silicon carbide (SiC), it is an ideal candidate for immobilization of noble gas fission products. Silicon carbide possesses excellent physical and chemical properties that make it a promising material, not only for advanced electronic devices (Raynaud 2001), but also for structural components in fusion reactors (Fenici et al. 1998; Nogami et al. 2009; Zhao et al. 2007; Wong et al. 2007; Katoh et al. 2007), a barrier for fission product diffusion in gas-cooled fission reactors (Kim et al. 2000), and an inert matrix for the transmutation of plutonium and other transuranics (Verrall et al. 1999; Krstic et al. 1996). The high thermal conductivity of SiC also enhances homogeneous heat distribution in devices and rapid heat transfer. Unlike traditional semiconductor materials, SiC has extremely low thermal diffusivities thereby limiting the migration of impurities. This low diffusivity for impurities is one of the reasons SiC is used as the fission product barrier in tri-structural-isotropic (TRISO) nuclear fuel and its use for this application has been demonstrated at temperatures over 2000 K (Schenk and Nabielek 1991; Schenk et al. 1990; Nabielek et al. 1990). Because of the low diffusivities for fission products and superior physical and chemical stability of SiC, it is an ideal candidate for immobilization of C, Kr, and Xe and perhaps other fission products, including I_2. Thermal release of helium generated in neutron-irradiated SiC does not occur until temperatures above 1200 K (Sasaki et al. 1991; Sasaki et al. 1989). Because of its low chemical reactivity, SiC is also proposed as cladding for advanced light water reactors (Filippov et al. 2007a, b; Filippov et al. 2006). A recent study showed evidence of pitting corrosion in □-SiC at 300°C, although no measurable mass loss occurred for exposure times up to 4000 hours. The microscopic evidence, however, indicates that even this stable material is somewhat susceptible to low-temperature corrosion involving volatile SiOH species (Henager Jr et al. 2008). While oxidation of SiC occurs at elevated temperatures, such oxide films generally form a barrier to further oxidation and should be negligible under conditions for immobilization unless significant water vapor is present (Opila 2003). Silicon carbide also occurs in nature as the extremely rare mineral moissanite (Bauer et al. 1963; Pierro et al. 2003), and SiC crystals of interstellar origin have been found in primitive meteorites (Alexander et al. 1990), both of which support its physical and chemical stability.

Since industrial scale fabrication of SiC monoliths with physical vapor deposition methods is a well-established technology (Abe et al. 2008; Jiangang et al. 2006; Saddow et al. 2001; Moon et al. 2001; Sugiyama et al. 1998), there is little, if any, technology development needed to produce dense, pure SiC. While there are many polymorphs of SiC, the cubic 3C structure is preferred for nuclear and structural applications, such as ceramic composite fibers and matrices and fine-grained coatings for TRISO nuclear fuel particles. Much of our knowledge of diffusivities of nuclear isotopes in SiC comes from studies of TRISO fuel particles (Peterson and Dunzik-Gougar 2006; Schenk et al. 1984; Smith 1979; Fukuda and Iwamoto 1978, 1976, 1975). Studies have shown that Xe and Kr have extremely low mobilities in SiC at

low temperatures and only become mobile above 1200°C (Fukuda and Iwamoto 1978, 1976, 1975). Thus, it appears that SiC is almost an ideal candidate material for storage and retention of volatile radioactive isotopes such ^{14}C, ^{85}Kr (and its companion Xe), and ^{129}I.

For immobilization of fission products, physical vapor deposition of monolithic 3C-SiC provides an industrial scale process from which to begin this development. It was anticipated that optimized physical vapor deposition (PVD) or chemical vapor deposition (CVD) technology with ion-assisted deposition would allow the synthesis of a SiC waste form with entrained radioactive C, Xe, I, and/or Kr. Captured carbon from reprocessing could supplement the carbon source used in processing, typically in the form of methyltrichlorosilane, CH_3SiCl_3 (Jiangang et al. 2006). Gaseous fission products, such as Xe and Kr, could be injected into the surface with low-energy ion guns or leaked into processing chamber (Grigorov and Martev 1988). One prior study indicated that up to 20 atomic% Ar could be entrained during PVD of Ti-films (Grigorov and Martev 1988). It is anticipated that equivalent amounts for Xe and Kr could be entrained within CVD or PVD SiC. Since Xe and Kr diffusivities are extremely low at ambient temperatures, the release rates of Xe and Kr are negligible, even along grain boundaries, for millions of years (Sauvage et al. 2007; Van Ginhoven et al. 2006; Pramono et al. 2004; Chen et al. 2000; Jung 1992; Fukuda and Iwamoto 1978, 1976).

5.2 Experimental Procedure:

5.2.1 Depositions

Silicon carbide targets were obtained and a 0.71-m box-coating chamber was outfitted for deposition with either a 75 mm (3”) Mity Mak circular magnetron sputtering cathode (target Saint Gobain SG-90 SiC-C composite) or a 100-mm rectangular unbalanced magnetron (UBM) cathode (target from Cerac, 99.5% SiC). A DynaVac IS1000 gridless, end-Hall type ion source was used for most of the Kr deposition, powered by an MDX Advanced Energy power supply. Per protocol in a research chamber, all surfaces in the chamber were covered with fresh stainless steel foil before this series of coatings to limit cross contamination with previous coating runs and to reduce arcing and debris generation during the ion-assisted depositions. Deliverable coatings were deposited on 50 mm diameter polished Si substrates mounted with clips in the center of a 200-mm diameter substrate holder. An anti-static N_2 gun was used to remove debris prior to loading in the coating chamber. An overnight pump-down was critical to reaching an ultimate chamber pressure of low1.3×10^{-5} to 1.3×10^{-6} Pa.

A summary of the depositions discussed in this report is given in Table 7. Initial depositions were performed with the substrate rotated directly over the target. A single leaf shutter was positioned between the target and the substrate to mask the substrate during target cleaning prior to the start of each deposition. It was then rotated toward the rear of the chamber to allow disposition on the substrate. Calibration runs were performed to determine the SiC deposition rate for a bonded SiC target with and without ion assist. The goal of the calibrations was to determine the substrate positioning that gave us the most uniform and highest deposition rate. For depositions with the 75 mm SiC target, the spacing between the substrate and the target was 127 mm. The ion gun was angled 30° toward the cathode/substrate

Figure 26. Initial ion gun deposition setup for SiC immobilization experiments with Kr.

(Figure 27) such that the ion flux would be co-incident with the primary ad-atom flux at the substrate material. For depositions with the UBM, the substrate/target gap was 89 mm, which is the optimum range of the UBM field. Figure 28 shows the initial setup with the UBM; it was later optimized for better ion-assist by rotating the UBM 90-deg and positioning the ion gun as used with the 75 mm depositions. Unfortunately, no photos were taken in that configuration.

The 75 mm SiC depositions were performed at a pressure of ~0.5 Pa (~4 mTorr) and 6×10^{-4} standard L/s (36 sccm) of either 100% Ar or Kr. An RF -10 power supply and in-house built matching network operating at 200 W and ~220-240 V for non-ion assist depositions were used. During the ion-assist depositions, the voltage dropped to 130-170 V for the same 200 W input due to interference from the ion gun. The ion gun neutralizer was set at ~19 V and 35 A to reduce arcing. The ion gun drive was set at either 0.05kW/120V (reduced cathode voltage to 150-170 V) or 0.1 kW/116 V (reduced cathode voltage to 130-150 V). The deposition time for 1 μm of either non-ion assist or IAD was approximately 200 min.

The UBM depositions utilized a PE 5000 AC Plasma power supply operating at 0.5 kW/0.75 A and ~700 V for non-ion assist depositions, with a 1 μm thick SiC film deposited in ~180 min. During IAD, the parameters were 0.3kW/0.5A and ~580V. The ion gun parameter for the UBM depositions were: neutralizer was 11.2 V/10 A; drive was 0.1 k W/215 V.

In order to obtain a free-standing powder of the material, depositions onto flakes of single crystal NaCl were attempted. The NaCl crystals were mounted on carbon tape with the addition of a SST mesh to prevent the crystals from falling off during deposition. The process of removing the film, dissolving the remaining salt, and drying the rinsed remaining material was unfortunately not successful. The salt dissolved as planned, but the SiC film reacted with and bonded to the drying crucible during a temperature excursion.

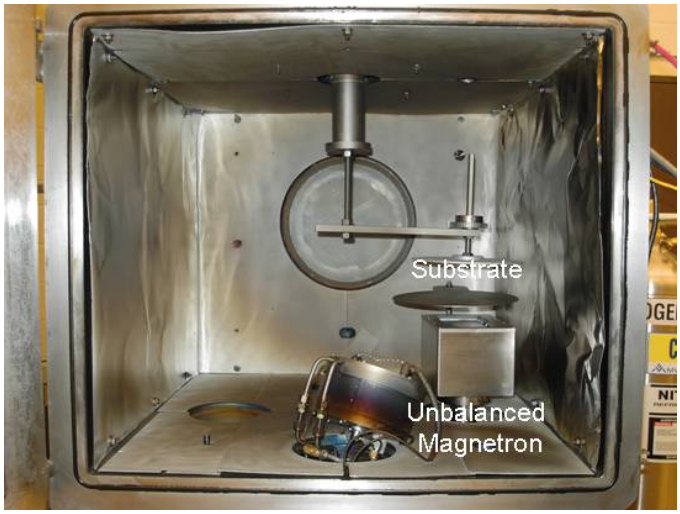

Figure 27. Unbalanced magnetron setup used for several Kr immobilization experiments

Table 5. Deposition information for selected samples.

Run #	Substrate	non-IAD	IAD	75 mm Cathode	UBM
Setup: substrate directly over 75 mm cathode, ion gun 30 degrees toward cathode					
1E-S	50 mm Si		X	X	
1G-S	50 mm Si	X		X	
1I-S	50 mm Si	X		X	
1K-S	50 mm Si		X	X	
1L-S	50 mm Si		X	X	
Setup: substrate directly over UBM cathode; PE 5000 AC power supply					
2G-S	50 mm Si		X		X
Setup: substrate directly over UBM cathode, PE 5000 AC power supply, ion gun and cathode positioned as shown in Figure 29					
2I-S	50 mm Si		X		X
Setup: UBM cathode rotated 90° , substrate directly over cathode; PE 5000 AC power supply; ion gun positioned directly in front of cathode					
2J-S	NaCl		X		X

5.2.2 Characterization

Three films were analyzed with a VersaProbe X-ray photoelectron spectrometer (XPS) system through the Environmental and Molecular Sciences Laboratory (EMSL) user facility at PNNL. Relative sensitivity factors from previous SiC depositions were used to quantify the Si, C, and O impurity levels in the materials. No standard material for krypton embedded in a solid matrix existed at the start of these experiments, so the literature relative sensitivity values for adsorbed krypton were used.

Rutherford backscattering (RBS) measurements were performed to accurately measure the composition of the film and the diffusion profiles of Kr (if any) after annealing at different temperatures. In these measurements, a 2.0 MeV Helium beam was used and the backscattered He ions from the samples were collected at the scattering angle of 150^{o}. The detailed RBS experimental conditions are shown in Table 5. The data were then fitted with a standard theoretical model with the SIMNRA (Mayer 1999) simulation code. This code utilizes the known Rutherford backscattering cross-section and all other experimental parameters shown in Table 6 together with the sample information to calculate the theoretical spectrum. In these simulations, the sample was divided into several thin layers of variable thickness and composition. Experimental parameters such as incident ion energy, atomic number of the ion, incident and scattering angles, energy calibration values for the detectors, solid angle of detection and the total charge deposited by the incident beam were input parameters. The density input was taken from literature values of films deposited in the same manner and characterized with glancing angle X-ray diffraction and spectroscopic ellipsometry. From this information and a trial sample structure, the program calculates the backscattered spectra. The composition profiles and film areal densities (in units of atoms/cm^2) are then

Table 6. The RBS analysis experimental conditions.

Experimental Parameters	Values
Incident Ion spices	Helium
Incident Ion Energy	2.0 MeV
Incident Angle	7°
Scattering Angle	150°
Charge	20 mC
Solid angle	1.5×10^{-3} steradians

systematically varied until the best fit to experiment is obtained. The areal density is the product of the atom number density of atoms and the film thickness.

Samples were successively annealed at 100, 200, 300, 400 and 500 ^{o}C for 30 minutes at each temperature. After each annealing step, samples were cooled to room temperature and RBS data were collected. The data representing the highest temperatures, therefore, had undergone several annealing steps.

5.3 Results

The initial deliverable depositions consisted of two coating structures, each with two approximately 1 μm thick layers. The first consisted of SiC deposited with 100% Ar as the sputtering gas capped by SiC deposited with 100% Kr as the sputtering gas. The second film consisted of the same argon-deposited base layer, but with the top deposition performed not only with Kr as the sputtering gas but with the addition of Kr applied with the ion source. The intent was to implant Kr into the structure with the acceleration of the ion source. Following these depositions, we also attempted several depositions with UBM sputtering. The UBM technique produces more energetic ad-atoms than traditional magnetron sputtering and tends to implant more of the sputtering gas into the structure. The ion gun was also used for these films, but may not have had much of an effect because it was shadowed by the UBM cathode, which requires a short working distance to produce the films.

Compositional analyses with XPS on three films (1I-S, 1L-S, and 2G-S) showed similar C/Si atomic ratios among the samples, slightly enriched in C over a pure SiC stoichiometry. This was expected for the 75 mm cathode, as the target SiC material used (Saint Gobain SG-90) was also C enriched by several atomic percent to maintain conductivity and, thus, good sputtering behavior. The UBM-deposited films were synthesized with a higher purity target, but research suggests that excess carbon may be preferred in amorphous SiC films.

In each case, the surface concentration of Kr was slightly higher than the bulk as seen in Figure 29. Resolving the reasons for this occurrence is one of the goals of the ongoing research, as it was also observed in the RBS data below. Further Ar milling and time spent under the ultra-high vacuum of the XPS instrument did not appreciably change the elemental composition of any of the films. In any event, the transient surface composition was not used for comparative purposes in preference of the more stable composition established with a 2 minute 2 kV Ar beam mill.

As expected, Sample 1I-S exhibited the lowest concentration of Kr of the three samples at 0.3 atomic% (1.4 mass%). The incorporation of sputtering ions into films is typically minimal due to the fact that most of the ion energy is taken up in the sputtering process. Trapping mechanisms and some bias-resputtering are typically thought to account for this low-level incorporation. The addition of Kr through an energetic ion source, however, produced dramatically different results. In this case (sample 1L-S), 1.6 atomic% (6.7 mass%) of Kr was incorporated into the bulk of the sample. The sample deposited with UBM exhibited similar results, with 1.3 atomic% (5.6 mass%) Kr incorporated into the film. This result is interesting because it was difficult to impinge the ion stream onto the growing film. It was thought that with a more favorable geometry, the results would be significantly improved.

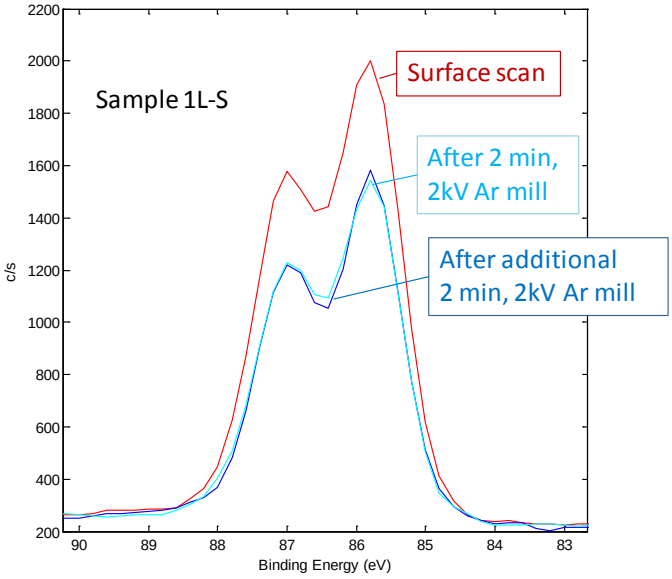

Figure 28. X-ray photoelectron spectra of the Kr 3d region showing Kr immobilized in sputtered SiC. This sample exhibited the maximum retention of 6.7 atomic% Kr (22 mass%).

This theory was tested in the film 2I-S. In this film, the UBM and ion gun were placed with a geometry that impinged the two sources at roughly the same point. Analysis by RBS revealed that this set up produced films with greater than 6.1 atomic% (>20 mass%) Kr loading in a thin layer (~40 nm thick) near the surface. This maximum was reached at a depth slightly into the film, while the surface (<10 nm) concentration was 4.5 atomic% (17.0 mass%). The majority of the film exhibited a constant 2.3 atomic% (9.3 mass%) loading.

This film was used to estimate the desorption of Kr with increasing temperature (Figure 29). The bulk concentration of Kr was unchanged throughout the experiment. The surface Kr exhibited a decrease in concentration after the 500°C 30 minute hold (and all preceding temperature anneals as well). The very surface decreased from 4.5 atomic% to 3 atomic% and the high-Kr layer decreased from 6.1 atomic% to 4 atomic%.

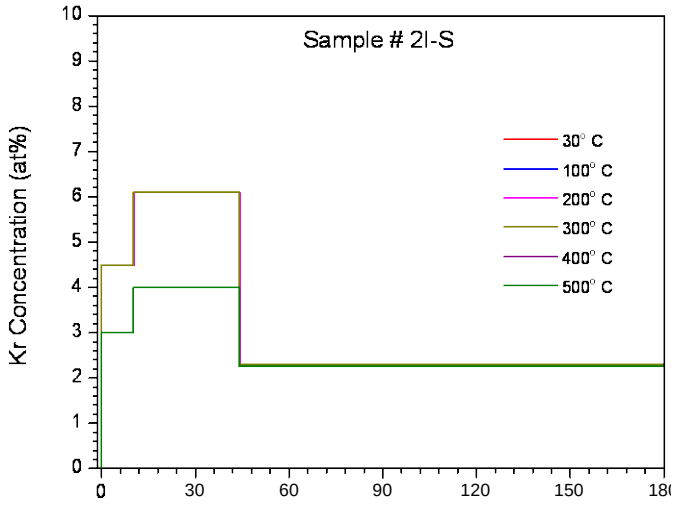

Figure 29. The RBS-generated depth profile of krypton concentration in SiC film during successive *in-situ* 30-minute heat treatments.

5.4 Conclusions

Stable Kr loadings of near 9.3 mass% were demonstrated in a non-optimized configuration. Layers of significantly higher loading (greater than 20 mass%) were also observed, suggesting that these levels or higher may be possible in an optimized process. The diffusion experiment data suggest that very limited

diffusion occurred in these materials at repository-relevant temperatures, confirming the conclusions in numerous literature reports. High temperature data did show some surface release, necessitating more detailed studies to determine the activation energy for Kr moving through the SiC matrix as a function of loading. There most certainly is a percolation threshold for Kr, above which diffusion is expected to be much more rapid. It does not appear that we have reached that level in these studies, however.

5.5 Future Work

The planned work will focus on several main tasks: optimization of waste loading, developing a predictive understanding of Kr diffusion as a function of loading, and the investigation of the immobilization of other key radionuclides, such as I_2 with this method.

In the first effort, a small ion implantation system (Peabody Scientific Ion Implanter System) with a 40 keV maximum acceleration has been made available to the project and has been installed on an available PVD chamber, as shown in Figure 30. We plan to repeat the earlier IAD runs without the small ion gun but with the ion implanter system operating at about 5 keV for the first deposits and gradually increase the ion energy to the 40 keV limit. The added energy and flux of the Kr produced with this tool should increase the percentage of Kr retained in the film as well as enabling the SiC structure to reconfigure to a stable state following implantation.

In the second effort, we will again use RBS as a tool, analyzing a matrix of films with a rage of waste loadings. With Kr loss measured with increasing temperature and time, a model of diffusion will be developed. In addition, the waste loading matrix will help us determine the maximum loading consistent with the storage requirements.

Third, we will demonstrate the applicability of this method towards other difficult-to-immobilize radionuclides. In addition to the noble gasses, ^{14}C, ^{129}I, and possibly ^{99}Tc may be immobilized in this manner given the proper separations. In particular, the team believes that I_2 is the next most straightforward volatile of concern and plans to demonstrate the implantation of non-radioactive I_2 in further experiments, followed by measurement of its vapor phase and aqueous stability in the host material.

Figure 30. Peabody Scientific ion implanter system (at left) attached to PVD deposition chamber (at right). The implanter is capable of beam energies from 2 to 40 keV with a Duoplasmatron ion source and low-pressure arc discharge system.

6. References

Abe, K, Y Nagasaka, T Kida, T Yamakami, R Hayashibe, and K Kamimura. 2008. "Characterization of Polycrystalline SiC Films Grown by HW-CVD Using Silicon Tetrafluoride." *Thin Solid Films* 516(5):637-40.

Ackley, RD, and Z Combs. 1973. *Applicability of Inorganic Sorbents for Trapping Radioiodine from Lmfbr Fuel Reprocessing Off-Gas*. Report No. ORNL/TM-4227, Oak Ridge National Laboratory, Oak Ridge, TN.

Alexander, CMOD, P Swan, and RM Walker. 1990. "In Situ Measurement of Interstellar Silicon Carbide in Two Cm Chondrite Meteorites." *Nature* 348(6303):715-17.

Bag, S, AF Gaudette, ME Bussell, and MG Kanatzidis. 2009. "Spongy Chalcogels of Non-Platinum Metals Act as Effective Hydrodesulfurization Catalysts." *Nature Chemistry* 1:217-24.

Bag, S, and MG Kanatzidis. 2010. "Chalcogels: Porous Metal-Chalcogenide Networks from Main-Group Metal Ions. Effect of Surface Polarizability on Selectivity in Gas Separation." *Journal of the American Chemical Society* 132(42):14951-59.

Bag, S, PN Trikalitis, PJ Chupas, GS Armatas, and MG Kanatzidis. 2007. "Porous Semiconducting Gels and Aerogels from Chalcogenide Clusters." *Science* 317(5837):490-93.

Bauer, J, J Fiala, and R Hrichova. 1963. "Natural -Silicon Carbide." *American Mineralogist* 48(5-6):620-34.

Bendixsen, CL, and FO German. 1975. *1974 Operation of the Icpp Rare Gas Recovery Facility*. Report No. ICP-1157, Allied Chemical Corporation, Idaho Falls, ID.

Bourrelly, S, PL Llewellyn, C Serre, F Millange, T Loiseau, and G Ferey. 2005. "Different Adsorption Behaviors of Methane and Carbon Dioxide in the Isotypic Nanoporous Metal Terephthalates Mil-53 and Mil-47." *Journal of the American Chemical Society* 127(39):13519-21. 10.1021/ja054668v.

Brown, RA, JD Christian, and TR Thomas. 1983. *Airborne Radionuclide Waste-Management Reference Document*. Report No. ENICO-1133, Exxon Nuclear Idaho Co., Inc., Idaho Falls, ID.

Chen, J, P Jung, and H Trinkaus. 2000. "Microstructural Evolution of Helium-Implanted -SiC." *Physical Review B (Condensed Matter)* 61(19):12923-32.

Dietzel, PDC, V Besikiotis, and R Blom. 2009. "Application of Metal-Organic Frameworks with Coordinatively Unsaturated Metal Sites in Storage and Separation of Methane and Carbon Dioxide." *Journal of Materials Chemistry* 19(39):7362-70. 10.1039/b911242a.

Fenici, P, AJF Rebelo, RH Jones, A Kohyama, and LL Snead. 1998. "Current Status of SiC/SiC Composites R&D." *Journal of Nuclear Materials* 258-263(pt A):215-25.

Férey, G, C Serre, T Devic, G Maurin, H Jobic, PL Llewellyn, G De Weireld, A Vimont, M Daturi, and JS Chang. 2011. "Why Hybrid Porous Solids Capture Greenhouse Gases?" *Chemical Society Reviews* 40(2):550-62. 10.1039/c0cs00040j.

Filippov, GA, EI Grishanin, MV Konditerov, VP Mastyukin, VI Mel'kin, VM Trubachev, LN Fal'kovskii, BI Fonarev, and GV Momot. 2006. "Investigation of the Corrosion Resistance of Fuel Micropellet Cladding Made of Silicon Carbide and Pyrolytic Carbon for the Operating Conditions of Light-Water Reactors in Nuclear Power Plants." *Atomic Energy* 101(4):722-29.

Filippov, GA, EI Grishanin, YE Lebedev, VM Trubachev, LN Fal'Kovskii, and BI Fonarev. 2007a. "Computational Estimate of the Corrosion Resistance of Fuel Microelements with Silicon Carbide Cladding in a Water Medium at Supercritical Pressure." *Atomic Energy* 102(3):204-10.

Filippov, GA, EI Grishanin, YE Lebedev, VM Trubachev, LN Fal'kovskii, and BI Fonarev. 2007b. "Erratum: Computational Estimate of the Corrosion Resistance of Fuel Microelements with Silicon

Carbide Cladding in a Water Medium at Supercritical Pressure (Atomic Energy (2007) 102:3 (204-210) Doi: 10.1007/S10512-007-0030-2)." *Atomic Energy* 102(4):329.

Fukuda, K, and K Iwamoto. 1975. "Diffusion and Evaporation of Fission Products in Coated Fuel Particles." *Journal of Nuclear Science and Technology* 12(3):181-9.

Fukuda, K, and K Iwamoto. 1978. "Diffusion Behavior of Fission Product in Pyrolytic Silicon Carbide." *Journal of Nuclear Materials* 75(1):131-44.

Fukuda, K, and K Iwamoto. 1976. "Xenon Diffusion Behaviour in Pyrolytic SiC. [Coating Material for Nuclear Fuel Particles]." *Journal of Materials Science* 11(3):522-8.

Gal, IJ, A Muk, M Todorovic, J Rajnvajn, D Cvjeticanin, L Vujisic, and MW First. 1974. Adsorption of Methyl Iodide on Impregnated Alumina. Presented at *13th AEC Air Cleaning Conference, CONF 740807,*

Gibbons, CS, VC Reinsborough, and WA Whitla. 1975. "Crystal Structures of K_2mgcl_4 and Cs_2mgcl_4." *Canadian Journal of Chemistry* 53:114-18.

Goossens, WRA, GG Eichholz, and DW Tedder, eds. 1991. *Treatment of Gaseous Effluents at Nuclear Facilities*. Harwood Academic Publishers, Chur, Newark, NJ.

Greathouse, JA, NW Ockwig, LJ Criscenti, TR Guilinger, P Pohl, and MD Allendorf. 2010. "Computational Screening of Metal-Organic Frameworks for Large-Molecule Chemical Sensing." *Physical Chemistry Chemical Physics* 12(39):12621-29. 10.1039/c0cp00092b.

Grigorov, GI, and IN Martev. 1988. "Inert Gas Entrapment in Films Produced by Ion-Assisted Physical Vapour Deposition Processes." *Thin Solid Films* 156(2):265-9.

Groenier, WS. 1985. Summary of United States Activities in Commercial Nuclear Airborne Waste Management. Presented at *the 18th DOE Nuclear Airborne Waste Management and Air Cleaning Conference (CONF-840806),* US Department of Energy, Washington, DC.

Haefner, DR, and TJ Tranter. 2007. *Methods of Gas Phase Capture of Iodine from Fuel Reprocessing Off-Gas: A Literature Survey*. Report No. INL/EXT-07-12299, Idaho National Laboratory, Idaho Falls, ID.

Hebel, W, and G Cottone. 1982. Management Modes for Iodine-129. In *Proceedings of a meeting organized by the Commission of the European Communities,*

Hebel, W, and G Cottone. 1983. Methods of Krypton-85 Management. In *Proceedings of a meeting organized by the Commission of the European Communities,*

Henager Jr, CH, AL Schemer-Kohrn, SG Pitman, DJ Senor, KJ Geelhood, and CL Painter. 2008. "Pitting Corrosion in CVD SiC at 300˚C in Deoxygenated High-Purity Water." *Journal of Nuclear Materials* 378(1):9-16.

Henrich, E. 1985. Selective Absorption of Noble Gases in Freon-12 at Low Temperatures and Atmospheric Pressure. Presented at *the 18th DOE Nuclear Air Cleaning Conference (CONF-840806),* US Department of Energy, Washington, DC.

Hruby, A. 1972. "Evaluation of Glass-Forming Tendency by Means of Dta." *Czechoslovak Journal of Physics, Section B* 22(11):1187-93.

IAEA. 1980a. *Radioiodine Removal in Nuclear Facilities: Methods and Techniques for Normal and Emergency Situations*. Report No. Technical Report Series No 201, International Atomic Energy Agency, Vienna, Austria.

IAEA. 1980b. *Separation, Storage and Disposal of Krypton-85*. Report No. Technical Report Series No 199, International Atomic Energy Agency, Vienna, Austria.

Izumi, J. 2003. *Handbook of Zeolite Science and Technology*. Marcel Dekker, New York, NY.

Jameson, CJ, AK Jameson, and HM Lim. 1997. "Competitive Adsorption of Xenon and Krypton in Zeolite Naa: Xe-129 Nuclear Magnetic Resonance Studies and Grand Canonical Monte Carlo Simulations." *Journal of Chemical Physics* 107(11):4364-72. 10.1063/1.474778.

Jiangang, D, N Singh, JB Summers, and CA Zorman. 2006. Development of Pecvd SiC for Mems Using 3ms as the Precursor. In *Proceedings of Silicon Carbide 2006-Materials, Processing and Devices. Symposium,* 283-8 pp. Materials Research Society,

Jung, P. 1992. "Diffusion and Retention of Helium in Graphite and Silicon Carbide." *Journal of Nuclear Materials* 191-94(pt A):377-81.

Kanatzidis, MG. 2011.

Kanatzidis, MG, and S Bag. 2008. "Semiconducting Aerogels from Chalcogenido Clusters with Broad Applications." USA US Patent No.

Katoh, Y, LL Snead, CH Henager Jr, A Hasegawa, A Kohyama, B Riccardi, and H Hegeman. 2007. "Current Status and Critical Issues for Development of SiC Composites for Fusion Applications." *Journal of Nuclear Materials* 367-370 A(SPEC ISS):659-71.

Kerry, FG. 2007. *Industrial Gas Handbook: Gas Separation and Purification*. CRC Press, Boca Raton, FL.

Kim, BG, Y Choi, JW Lee, YW Lee, DS Sohn, and GM Kim. 2000. "Multi-Layer Coating of Silicon Carbide and Pyrolytic Carbon on UO2 Pellets by a Combustion Reaction." *Journal of Nuclear Materials* 281(2-3):163-70.

Kitaura, R, F Iwahori, R Matsuda, S Kitagawa, Y Kubota, M Takata, and TC Kobayashi. 2004. "Rational Design and Crystal Structure Determination of a 3-D Metal-Organic Jungle-Gym-Like Open Framework." *Inorganic Chemistry* 43(21):6522-24. 10.1021/ic049005d.

Krstic, VD, MD Vlajic, and RA Verrall. 1996. "Silicon Carbide Ceramics for Nuclear Application." *Key Engineering Materials* 122-124:387-96.

Kusz, J, and D Kucharczyk. 1995. "The Comparative Study of the Commensurate Structure of K_2zncl_4." *Applied Crystallography* 6:268-72.

Lee, J, OK Farha, J Roberts, KA Scheidt, ST Nguyen, and JT Hupp. 2009. "Metal-Organic Framework Materials as Catalysts." *Chemical Society Reviews* 38(5):1450-59. 10.1039/b807080f.

Leigh, IW. 1994. *International Nuclear Waste Management Fact Book*. Report No. PNL-9450-1, United States.

Li, H, M Eddaoudi, M O'Keeffe, and OM Yaghi. 1999. "Design and Synthesis of an Exceptionally Stable and Highly Porous Metal-Organic Framework." *Nature* 402(6759):276-79.

Li, JR, RJ Kuppler, and HC Zhou. 2009. "Selective Gas Adsorption and Separation in Metal-Organic Frameworks." *Chemical Society Reviews* 38(5):1477-504. 10.1039/b802426j.

Lillo-Ródenas, MA, AJ Fletcher, KM Thomas, D Cazorla-Amorós, and A Linares-Solano. 2006. "Competitive Adsorption of a Benzene-Toluene Mixture on Activated Carbons at Low Concentration." *Carbon* 44(8):1455-63. 10.1016/j.carbon.2005.12.001.

Little, DK. 1983. Noble Gas Removal and Concentration by Combining Fluorocarbon Absorption and Adsorption Techniques. Presented at *the 17th DOE Nuclear Air Cleaning Conference (CONF-820833),* US Department of Energy, Washington, DC.

Maeck, WJ, and DT Pence. 1970. Application of the Metal Zeolites to Radioactive Air Cleaning Problems. Presented at *11th AEC Air Cleaning Conference, CONF-700816,*

Mayer, M. 1999. "Simnra, a Simulation Program for the Analysis of Nra, Rbs and ERDA." In *Application of Accelerators in Research and Industry, Pts 1 and 2,* eds. JL Duggan and IL Morgan, Vol 475, pp. 541-44.

Moon, CK, HJ Song, JK Kim, JH Park, SJ Jang, JB Yoo, HR Park, and B-T Lee. 2001. "Chemical-Vapor-Deposition Growth and Characterization of Epitaxial 3C- SiC Films on Soi Substrates with Thin Silicon Top Layers." *Journal of Materials Research* 16(1):24-27.

Mueller, U, M Schubert, F Teich, H Puetter, K Schierle-Arndt, and J Pastre. 2006. "Metal-Organic Frameworks - Prospective Industrial Applications." *Journal of Materials Chemistry* 16(7):626-36.

Nabielek, H, W Kuhnlein, W Schenk, W Heit, A Christ, and H Ragoss. 1990. "Development of Advanced HTR Fuel Elements." *Nuclear Engineering and Design* 121(2):199-210.

Naruki, F. 1985. Research and Development on Air Cleaning Systems of Reprocessing Plant in Japan. Presented at *the 18th DOE Nuclear Airborne Waste Management and Air Cleaning Conference (CONF-840806)*, US Department of Energy, Washington, DC.

Nogami, S, A Hasegawa, T Murayama, N Otake, M Satou, and K Abe. 2009. "Compatibility between SiC and Li Ceramics for Solid Breeding Blanket System." *Journal of Nuclear Materials* 386-388(C):628-30.

Oh, Y, S Bag, CD Malliakas, and MG Kanatzidis. 2011. "Selective Surfaces: High-Surface-Area Zinc Tin Sulfide Chalcogels." *Chemistry of Materials* 23(9):2447-56.

Ohba, S, S Sato, Y Saito, K-i Ohshima, and J Harada. 1983. "Electron-Density Distribution in Crystals of Potassium Tetrachloroplatinate(Li) and Influence of X-Ray Diffuse Scattering." *Acta Crystallographica* B39:49-53.

Ohtsuka, K. 1997. "Preparation and Properties of Two-Dimensional Microporous Pillared Interlayered Solids." *Chemistry of Materials* 9(10):2039-50. 10.1021/cm9605227.

Opila, EJ. 2003. "Oxidation and Volatilization of Silica Formers in Water Vapor." *Journal of the American Ceramic Society* 86(8):1238-48.

Pankratz, LB. 1982. *Thermodynamic Properties of Elements and Oxides*. 672, U.S. Department of the Interior, Bureau of Mines, Washington, D.C.

Pankratz, LB. 1984. *Thermodynamic Properties of Halides*. 674, U.S. Department of the Interior, Bureau of Mines, Washington, D.C.

Parr, RG, and RG Pearson. 1983. "Absolute Hardness: Companion Parameter to Absolute Electronegativity." *Journal of the American Chemical Society* 105:7512-16.

Pearson, RG. 1997. *Chemical Hardness*. WILEY-VCH Verlag GmbH, Weinheim, Germany.

Pearson, RG. 1963. "Hard and Soft Acids and Bases." *Journal of the American Chemical Society* 85(22):3533-39.

Pence, DT, FA Duce, and WJ Maeck. 1972. Developments in the Removal of Airborne Iodine Species with Metal Substituted Zeolites. Presented at *12th AEC Air Cleaning Conference, CONF 720823,*

Pence, DT, FA Duce, and WJ Maeck. 1970. Study of the Adsorption Properties of Metal Zeolites for Airborne Iodine Species. Presented at *11th AEC Air Cleaning Conference, CONF 700816,*

Peterson, J, and ML Dunzik-Gougar. 2006. "Degradation of TRISO Fuel in a Repository Environment." *Transactions of the American Nuclear Society* 94:668-9.

Pierro, SD, E Gnos, BH Grobety, T Armbruster, SM Bernasconi, and P Ulmer. 2003. "Rock-Forming Moissanite (Natural A-Silicon Carbide)." *American Mineralogist* 88:1817-21.

Pinchback, TR, JR Winkel, DK Matlock, and DL Olson. 1981. "Corrosion of Structural Alloys in Liquid Rubidium." *Nuclear Technology* 54(2):201-07.

Pramono, Y, K Sasaki, and T Yano. 2004. "Release and Diffusion Rate of Helium in Neutron-Irradiated SiC." *Journal of Nuclear Science and Technology* 41(7):751-55.

Raynaud, C. 2001. "Silica Films on Silicon Carbide: A Review of Electrical Properties and Device Applications." *Journal of Non-Crystalline Solids* 280(1-3):1-31.

Riley, BJ, J Chun, JV Ryan, J Matyáš, XS Li, DW Matson, SK Sundaram, DM Strachan, and JD Vienna. 2011. "Chalcogen-Based Aerogels as a Multifunctional Platform for Remediation of Radioactive Iodine." *RSC Advances*. DOI:10.1039/C1RA00351H.

Rowsell, JLC, EC Spencer, J Eckert, JAK Howard, and OM Yaghi. 2005. "Gas Adsorption Sites in a Large-Pore Metal-Organic Framework." *Science* 309(5739):1350-54. 10.1126/science.1113247.

Ruffolo, D, and P Boolchand. 1985. "Origin of Glass Formation." *Physical Review Letters* 55(2):242-45.

Ryan, P, OK Farha, LJ Broadbelt, and RQ Snurr. 2011. "Computational Screening of Metal-Organic Frameworks for Xenon/Krypton Separation." *Aiche Journal* 57(7):1759-66. 10.1002/aic.12397.

Saddow, SE, TE Schattner, J Brown, L Grazulis, K Mahalingam, G Landis, R Bertke, and WC Mitchel. 2001. "Effects of Substrate Surface Preparation on Chemical Vapor Deposition Growth of 4H- SiC Epitaxial Layers." *Journal of Electronic Materials* 30(3):228-34.

Sasaki, K, T Maruyama, and T Iseki. 1989. "Helium Release from Neutron-Irradiated SiC Containing 10b Isotope." *Journal of Nuclear Materials* 168(3):349-51.

Sasaki, K, T Yano, T Maruyama, and T Iseki. 1991. Helium Release and Microstructure of Neutron-Irradiated SiC Ceramics. In *Proceedings* 407-10 pp.

Sauvage, T, G Carlot, G Martin, L Vincent, P Garcia, MF Barthe, A Gentils, and P Desgardin. 2007. "Helium Behavior in -SiC Ceramics Investigated by Nra Technique." *Nuclear Instruments and Methods in Physics Research, Section B: Beam Interactions with Materials and Atoms* 257(1-2 SPEC. ISS.):231-35.

Schenk, W, and H Nabielek. 1991. "High-Temperature Reactor Fuel Fission Product Release and Distribution at 1600 to 1800C." *Nuclear Technology* 96(3):323-36.

Schenk, W, A Naoumidis, and H Nickel. 1984. "Behaviour of Spherical HTR Fuel Elements under Accident Conditions." *Journal of Nuclear Materials* 124(3):25-32.

Schenk, W, G Pott, and H Nabielek. 1990. "Fuel Accident Performance Testing for Small HTRs." *Journal of Nuclear Materials* 171(1):19-30.

Smith, CL. 1979. "SiC-Fission Product Reactions in HTGR TRISO UC_2 and UC_xO_y Fissile Fuel. II. Reactions under Isothermal Conditions." *Journal of the American Ceramic Society* 62(11-12):607-13.

Sugiyama, N, A Okamoto, K Okumura, T Tani, and N Kamiya. 1998. "Step Structures and Dislocations of SiC Single Crystals Grown by Modified Lely Method." *Journal of Crystal Growth* 191(1/2):84-91.

Thallapally, PK, J Tian, MR Kishan, CA Fernandez, SJ Dalgarno, PB McGrail, JE Warren, and JL Atwood. 2008. "Flexible (Breathing) Interpenetrated Metal-Organic Frameworks for CO(2) Separation Applications." *Journal of the American Chemical Society* 130(50):16842-+. 10.1021/ja806391k.

Thomas, TR, LP Murphy, BA Staples, and JT Nichols. 1977. *Airborne Elemental Iodine Ioading Capacities of Metal Zeolites and a Method for Recycling Silver Zeolite*. Report No. ICP-1119, Idaho National Laboratory, Idaho Falls, ID.

Van Ginhoven, RM, A Chartier, C Meis, WJ Weber, and LR Corrales. 2006. "Theoretical Study of Helium Insertion and Diffusion in 3C-SiC." *Journal of Nuclear Materials* 348(1-2):51-59.

Vermin, WJ, GC Verschoor, and DJW Ijdo. 1976. "Two Modifications of Cobalt Dipotassium Tetrachloride." *Acta Crystallographica* B32:3325-28.

Verrall, RA, MD Vlajic, and VD Krstic. 1999. "Silicon Carbide as an Inert-Matrix for a Thermal Reactor Fuel." *Journal of Nuclear Materials* 274(1):54-60.

Visser, D, GC Verschoor, and DJW Ijdo. 1980. "The Structure of $KNiCl_3$ at Room Temperature." *Acta Crystallographica* B36:28-34.

Wong, CPC, V Chernov, A Kimura, Y Katoh, N Morley, T Muroga, KW Song, YC Wu, and M Zmitko. 2007. "ITER-Test Blanket Module Functional Materials." *Journal of Nuclear Materials* 367-370(1):1287-92.

Zhao, J, G Wang, Q Guo, and L Liu. 2007. "Microstructure and Property of SiC Coating for Carbon Materials." *Fusion Engineering and Design* 82(4):363-68.